university of groningen / faculty of science and engineering

UNIVERSITY OF TWENTE.

Modelling of EM sensor and investigation of AISI 420 microstructure for non-destructive testing

Egge Rouwhorst

February 28, 2023

Supervisors:
Prof. Dr. Y.T. Pei
Dr. habil C. Soyarslan
Dr. ir. R. van Tijum

Affiliation:
RUG
UT
Philips

Abstract

The microstructure of a material governs the mechanical as well as the magnetic properties. On this basis then, a measurement of the magnetic properties yields information about the mechanical properties. Being able to measure non-destructively the quality of the material is an important step towards industry 4.0. Eddy current sensors generate a magnetic field and measure the disturbance caused by the presence of a flaw in the material being tested. Previous internal experiments showed that different hardnesses and tensile strengths are distinguishable for AISI 420. The physics behind this is however not well understood and the relation with the underlying microstructure is unclear. Both are hence researched. A gyrator-capacitor model of the sensor was created and validated. The effect of work hardening on the sensor response was investigated with in- and ex-situ tensile tests and combined with VSM, EBSD and MFM measurements. The largest contributors to the sensor output were found to be stresses and initial dislocation density due to plastic deformation. Residual stresses are most likely responsible for an extra decrease of inductance on top of the reduction due to dislocation formation.

Contents

1 Introduction

To ensure quality of products and minimize waste, it is desirable for a production line to have steel with well specified properties. In practice the delivered material does not always meet the criteria and tightening the specifications drives up the material cost. Conventional methods to determine material parameters are often time consuming and destructive. Non-destructive testing is therefore of great interest, besides the prospects of combining it with the process control. One of the options for non-destructive testing is an electromagnetic (EM) sensor, which can measure contactless and quick. The mechanical, electrical and magnetic properties are governed by the microstructure of a material, like composition, phase, precipitates and grain information. Information in one domain can therefore tell something about the other domain. A plethora of studies have shown the magnetic properties can be correlated with the mechanical ones, see for example [1, 2, 3, 4] among others. This study focusses on a specific eddy current sensor and its output, which is the phase and gain of the receiver coil for various frequencies. The main goal of this research is to better understand the sensor output and identify its relation to the material microstructure. To limit the scope, the effect of work hardening on the sensor output and on the microstructure will be investigated. This study is restricted to the material AISI 420, a martensitic stainless steel. First a relatively quick overview of microstructural magnetism is given, followed up by analytical models of the sensor. Various measurements, of which are Electron Back Scatter Diffraction (EBSD), resistivity, permeability and Magnetic Force Microscope (MFM) measurements, are performed to validate this model and to understand the sensor output and material behaviour. An overview of the relevant relations to couple the the sensor output with the microstructure is given in figure 1.1. The relations between the blocks are phenomenological and for most relations a quantitative relation is very hard to make. So is for example modelling the magnetization in a magneto-mechanical coupled manner still a very active area in research [5, 6].

Phenomenological flowchart

For a ferromagnetic material with constant material content and temperature.

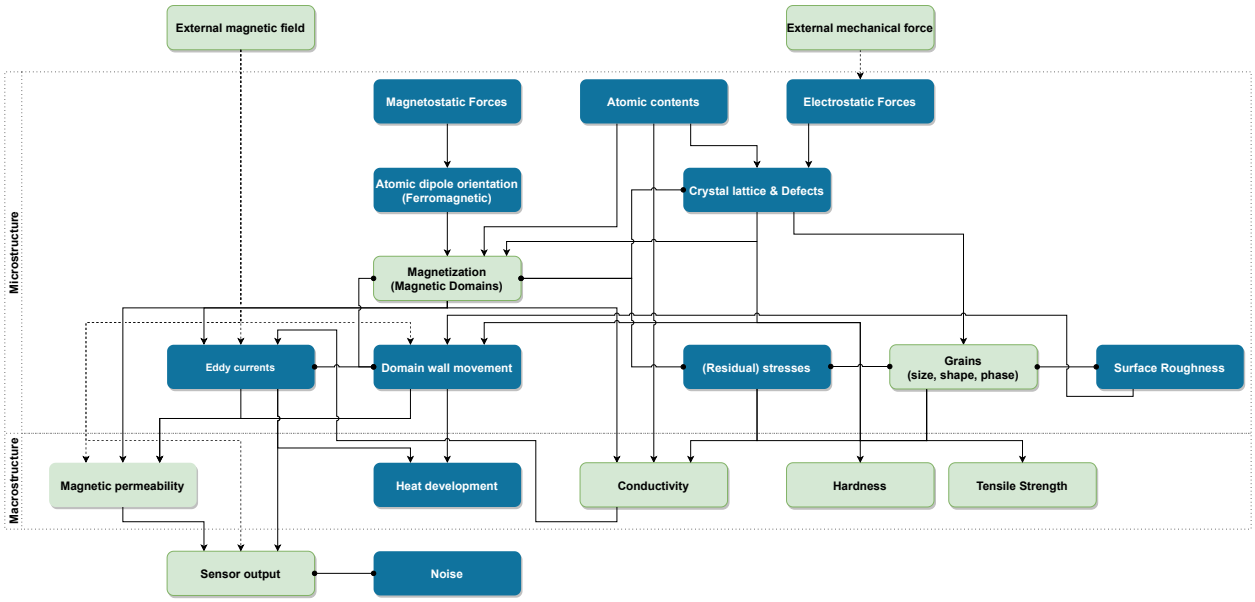

Figure 1.1: Overview of most of the relevant relations. Green blocks indicate reasonably controllable or measurable properties. Arrows indicate a relation from the tail to the head and lines with dots indicate a mutual relation.

2 Theory of Magnetism

This section is only meant as a relatively quick overview of the theory of magnetism. For this, use has been made of the books of R. Bozorth, S. Chikazumi and B.D. Cullity [7, 8, 9]. Many phenomena highlighted here can be explained in terms of energy minimization and complicated calculations can be done to explain or predict them. Those calculations and more in-depth information can be found in the aforementioned books.

2.1 Atomic origin of magnetism

It is well known that magnets have a north and a south pole. Different, or opposite poles attract and like poles repel, much like the electric forces. Trying to isolate a pole by, for example, cutting a bar magnet in half, will result in disappointment as well as two magnets. A magnet can be viewed as a large collection of very small magnets, all aligned, adding all the individual magnetic moments. This picture is not far from the truth. On the atomic level, nuclei and electrons possess intrinsic magnetic moments due to spin and additionally the electrons orbital motion adds to the magnetic moment. The magnetic moments of the nuclei are negligible since nuclei are much heavier. Electrons in an atom can pair up with opposite spin and orbital angular momentum and cancel the magnetic moments. Generally therefore, atoms with full shells have no atomic magnetic moment. However, predicting the magnetic moment of a sample of atoms from the individual atomic magnetic moments is challenging. There are two distinct theories on this matter. One is the localized momentum theory, used in the molecular field theory which views the electrons as attached to atoms. The band theory abandons this idea and considers the outermost electrons as part of the crystal as a whole. Both of these theories have their merits.

Several magnetic behaviours can be distinguished based on the alignment of magnetic moments of atoms such as diamagnetic, paramagnetic and ferromagnetic. For ferromagnetic materials the magnetic moments of neighbouring atoms all align parallel, creating a strong magnetic moment. Crystal structure causes certain direction to be a most favourable alignment, called the 'easy' axis of magnetization.

2.2 Magnetic fields

Permanent magnets and moving charges give rise to a magnetic field $\mathbf{H}$, called the magnetic field strength or the H-field with unit A/m. When a magnetic moment is inside a field, a torque is applied to align the magnetic moment with the field. If a uniform field is applied to a collection of atoms, the magnetic moments start to align. The intensity of magnetization $\mathbf{M}$ is simply the vectorial sum of the magnetic moments in a unit volume and has as unit Tesla ($\mathrm{T} = \mathrm{N\,A^{-1}\,m^{-1}}$)[1]. The magnetic flux density $\mathbf{B}$ is defined as:

$$\mathbf{B} = \mu_0(\mathbf{M} + \mathbf{H}), \tag{2.1}$$

[1]Note that in some texts cgs units such as Oersted and Gauss instead of the Ampere per meter and Tesla are used, giving rise to different factors and additional confusion. Moreover, for the H-field sometimes B-field units are used by multiplying with μ_0.

where μ_0 is the permeability of vacuum, approximately $4\pi \cdot 10^{-7}\,\mathrm{N/A^2}$. Setting the magnetization proportional to the applied field as:

$$\mathbf{M} = \chi \mathbf{H}, \tag{2.2}$$

with magnetic susceptibility χ and combining these two relations gives:

$$\begin{aligned} \mathbf{B} &= \mu_0(\chi + 1)\mathbf{H} \\ &= \mu \mathbf{H}, \end{aligned} \tag{2.3}$$

with the total magnetic permeability μ. Often the relative permeability μ_r is used, defined as:

$$\mu_\mathrm{r} = \mu/\mu_0 = \chi + 1. \tag{2.4}$$

In many weakly magnetic materials such as diamagnetic or paramagnetic the susceptibility is mostly constant and small, but in ferromagnetic materials the magnetization has a non-linear relation with the H-field and susceptibility can become very large.

When a magnetic field is applied to a specimen and the magnetic moments align, there is an additional effect as the poles on the ends will create an opposing field which is called a *demagnetizing field*. This effect depends on the intensity of magnetization and the shape of the specimen. Since it depends on the shape, it needs to be corrected for if one wants the true, shape independent, magnetization and permeability. The demagnetizing field H_d is given as:

$$H_\mathrm{d} = N_\mathrm{d} M/\mu_0, \tag{2.5}$$

with N_d the demagnetizing factor, depending only on the shape of the sample. The effective magnetic field inside the material is then given as $H_\mathrm{eff} = H - H_\mathrm{d}$. For a thin plate the demagnetization factor is close to 1 when magnetized in the perpendicular direction and close to 0 for magnetization in the direction parallel to its surface [8, 9].

2.3 Domain theory

As stated in section 2.1, the magnetic moment of atoms in ferromagnetic materials align parallel. However, not all ferromagnetic materials have a magnetization by default, they are not permanent magnets. This is because throughout the material there are regions, domains, which need not have their magnetization aligned, see figure 2.1a. Between domains there is then a domain wall in which the atomic magnetic moments rotate from one orientation to another over the thickness of the wall. Domain walls are said to be 180° walls when the magnetic moments make a 180° angle and are said to be 90° walls for any other angle. Which angles occur depends on the crystal structure. A common configuration is where domains are capped off by so called closure domains with 90° walls. Two types of rotation can be distinguished for 180° walls: rotation in- and out- of the plane of the domain wall, called Bloch and Néel wall respectively. Bloch walls are the most common domain walls. Domain walls tend to be straight along the direction of magnetization as otherwise magnetic poles would appear, which act as a restoring force, they can more easily curve in the direction perpendicular to the magnetization, as depicted in figure 2.1b.

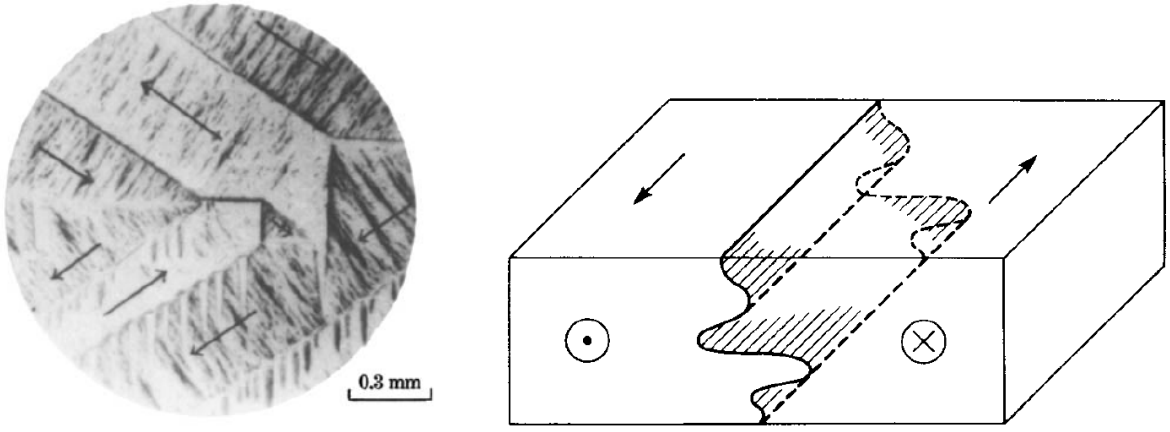

(a) A domain pattern [8]. (b) Possible curvature of a domain wall [8].

Figure 2.1: Domain and domain wall visualizations.

Domain walls tend to occur at inhomogeneities such as grain boundaries, voids and dislocations. It is not the case that grain boundaries imply a domain wall, in fact, domains can be more or less continuous across grains. Magnetization in domain theory is explained by two mechanisms: domain wall displacement and domain rotation. When a magnetic field is switched on near a material, the domains in the direction of the applied field will grow at the expense of the domains pointing in opposite direction. This growth is synonymous with the domain wall displacement. Whether the two mechanisms occur simultaneously or in a certain order depends on the material and the hindrances to the mechanism. Wall displacement is hindered by inhomogeneities, domain rotation is only affected by the materials magnetic anisotropy.

2.4 Hysteresis

When varying the field strength, ferromagnetic material such as iron responds differently depending on the field strength. At very low field strengths of 3 mA/m to 3 A/m it was found by Rayleigh that the permeability was constant. For higher field strengths of 6.4 A/m to 96 A/m a phenomena appears where the magnetic flux density lags the applied field strength and the permeability varied linearly with H according to the Rayleigh law:

$$\mu = \mu_{\mathrm{i}} + \eta H, \tag{2.6}$$

with μ_{i} the initial permeability and η is called the Rayleigh constant. The region of field strength for which this relation applies is commonly called the *Rayleigh region*. The corresponding Rayleigh loop with maximum applied field H_m can then be described by two parabolas:

$$B = (\mu_i + \eta H_m)H \pm \frac{\eta}{2}(H_m^2 - H^2), \tag{2.7}$$

where the plus and minus sign describe the descending and ascending part of the loop.[2]

[2]It turns out that at very low values of H this description leads to unphysical predictions and a slight modification is required [10].

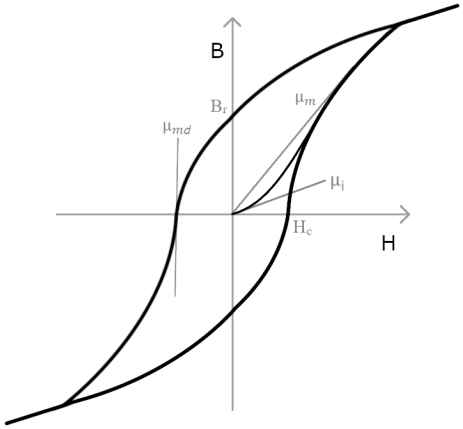

Figure 2.2: A typical B-H curve.

At even higher fields the permeability can vary more drastically. A plot of a typical high field magnetization curve, called a B-H curve, can be seen in figure 2.2. Several quantities can be obtained from this curve, for example the *remanence* B_r or the *coercive field* H_c, corresponding to the magnetic flux density at $H = 0$ and the magnetic field strength corresponding to $B = 0$ respectively. These two quantities are most commonly used for the material in the limit of the high field as these values approach a limiting value there. It can be seen that the magnetic flux lags behind the applied field as it depends on the material history, this is called *hysteresis* and this loop is called a hysteresis loop. The permeability is the slope of the curve and several kinds of permeability can be distinguished like the *initial*, *maximum* and *normal* permeability. Initial permeability μ_i is the slope when starting from the origin. Maximum permeability, μ_m is the steepest slope connecting the origin with the graph when increasing H from 0 and normal or *differential* permeability is the slope of the loop at any point. Of course then there is also a maximum differential permeability μ_md. As can be seen in the figure, the slope at high magnetic field strength becomes a constant non-zero value, this is because magnetizing a material can only go so far, since at some point all the magnetic moments will have fully aligned, which is called the *saturation magnetization* M_s. The magnetization and hence the permeability will then take a constant value. In many cases it is more appropriate to plot a M-H curve, correcting for the B-field due to the H-field and isolating the material response.

2.5 Magneto-mechanical coupling

It is known that the shape of a material might change slightly due to an applied magnetic field. This effect is called *magnetostriction*, λ, and can be written as:

$$\lambda = \frac{\Delta l}{l}, \tag{2.8}$$

where the length l and the change of length Δl are in the direction of the applied field. The value of λ increases with the applied field strength and may differ in sign and magnitude

depending on the crystallographic direction. Because of the dependence of crystallographic direction, the displacement of 180° domain walls do not contribute to magnetostriction. In polycrystalline materials with random crystallographic directions, the magnetostriction averages out throughout the material and becomes isotropic [8].

The origin of magnetostriction is mainly due to spin-orbit coupling and is crudely visualised with oval shaped electron clouds in figure 2.3. The black dots represent nuclei and the arrows the magnetic moments. When a field is applied the electron clouds align, which means the inter-atomic distance becomes slightly smaller.

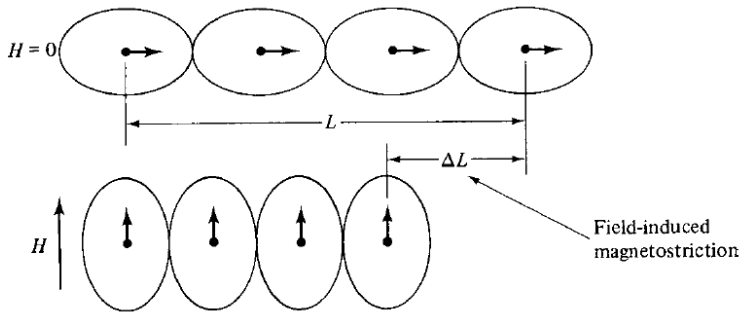

Figure 2.3: Schematic depiction of magnetostriction [9].

With magnetostriction there is also a superimposed effect called the *form effect*, in which the length changes due to the appearance of magnetic poles and the demagnetizing field. This effects depends on the shape of the specimen, like the demagnetizing effect.

Inverse magnetostriction, also called the *Villari effect*, is the phenomena that the magnetic properties change based on applied stress. If a material has positive magnetostriction and is brought under tension, domains parallel to the tensile stress grow at the cost of domains at right angles. As a result the material is more easily magnetized in the direction of tension than without tension. Compression makes magnetization more difficult with positive magnetostriction. The inverse magnetostriction combined with the fact that 180° domain walls do not contribute to this causes the initial magnetization by wall motion to occur predominantly by 180° wall motion, given there are no residual stresses. If there are stresses, 90° wall motion might very well precede 180° wall motion [11].

2.6 Domain wall motion hindrances

Inclusions, such as second phase particles (precipitates), impurities, voids or generally regions with locally a drastically lower permeability act as natural places for a domain wall to be in, as the free poles due to the inclusion are in a more energy favourable position within a wall. Stresses, for example existing due to dislocations and magnetostriction, also affect the domain wall motion via the Villari effect, as discussed above. Due to these hindrances, the domain wall movement can be irreversible. This effect can be depicted in terms of an energy landscape for the domain wall. In figure 2.4, an example of such landscape is depicted with the energy and energy gradient on the y-axis. With no applied field, the wall is at an energy minimum. Increasing the field moves the wall reversibly from position 1 to 2, where the energy has the steepest gradient, i.e., the largest restoring force. Increasing the field

beyond this point means there is enough force from the field to overcome the obstacle, and the wall will snap irreversibly to the next biggest gradient at position 3. Reducing the field to zero from point 3 will move the wall to point 4, the local energy minimum. Reversing the field enough will cause the wall to jump from point 5 to 6. The sudden, discontinuous jump from the wall is called the *Barkhausen effect*. Physically, an example of such jump is a wall existing between two inclusions, bulging in the middle and eventually snapping loose with increasing field strength. The supplied energy for a Barkhausen jump to occur does not necessarily need to come from a magnetic field but can also come from the Villari effect or thermal fluctuations.

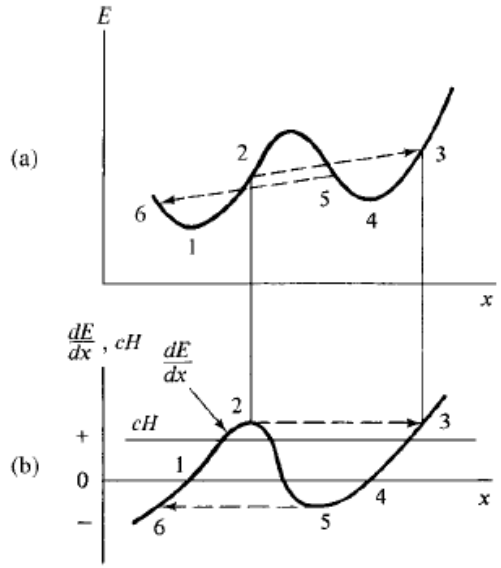

Figure 2.4: Energy landscape for domain wall motion [9]

.

2.7 Alternating field

So far, the magnetic field was treated separately from the electric field, but we know they are closely intertwined. When the magnetic field changes, it will induce an electromotive force (e.m.f.) $\mathcal{E}$ according to Lenz' law:

$$\mathcal{E} = -\frac{d\Phi_B}{dt}, \tag{2.9}$$

$$\Phi_B = \iint_S B. \tag{2.10}$$

Φ_B is hence the magnetic flux through a surface S. The e.m.f. causes a current to flow, which in turn causes a magnetic field, opposing the initial flux. The induced current is called *eddy current*. The eddy currents will flow in concentric loops around the place of the applied magnetic field. Because the eddy currents generate a magnetic field inside their loops, the opposing magnetic field is strongest in the middle. If the induced current is strong enough, the magnetic field in the middle of the loop can be completely cancelled, which means the

eddy currents mainly flow in an annulus as seen in figure 2.5. Furthermore, because of the same effect the magnetic field will be damped in the bulk of the material and lag behind that of the surface, which is visible in the 500 Hz picture of figure 2.5. If an alternating magnetic field is applied with frequency f, the depth at which the amplitude of the magnetic flux decreases to $1/e$ is called the skin depth s and is often given as:

$$s = \sqrt{\frac{\rho}{\pi f \mu}}, \tag{2.11}$$

with ρ the electrical resistivity in $\Omega\,\mathrm{m}$.[3]

An alternating magnetic field will move the domain walls back and forth and oscillate the direction of magnetization of the domains. In strongly magnetic materials, such as iron, wall motion is predominant at low frequencies. Microscopically, the permeability can vary greatly because of this. Consider a change in magnetic field ΔH that moves a domain wall some distance, but does not rotate the domains. Outside of the region in which the wall moved the magnetization will not have changed, meaning $\mu = \Delta B/\Delta H = \mu_0$. Inside the region the magnetization did change, meaning $\mu = \mu_0(1 + 2M_\mathrm{s})$. Permeability can therefore perhaps be better thought of as a macroscopic property. Additionally, the domain wall displacement is a change of magnetization, meaning that also there a back-e.m.f. will be generated, creating microscopic eddy currents, inducing additional opposition of the applied field. This effect can be seen as a damping of the wall displacement. The lag of the material B-field response to a H-field is the result of damping, i.e. energy loss. This lag can be characterised with a complex permeability. However, since the eddy currents and hence damping depends on the shape of the specimen, this does not seem like a useful method for generalization. In many texts the power losses are separated into hysteresis losses and eddy current losses, although physically these have the same origin of loss due to domain wall motion [9].

[3] Some caution has to be used with the formula, as the formula seems to be mainly applicable in situations where the field is parallel to the materials surface, not perpendicular as in case of this research [12].

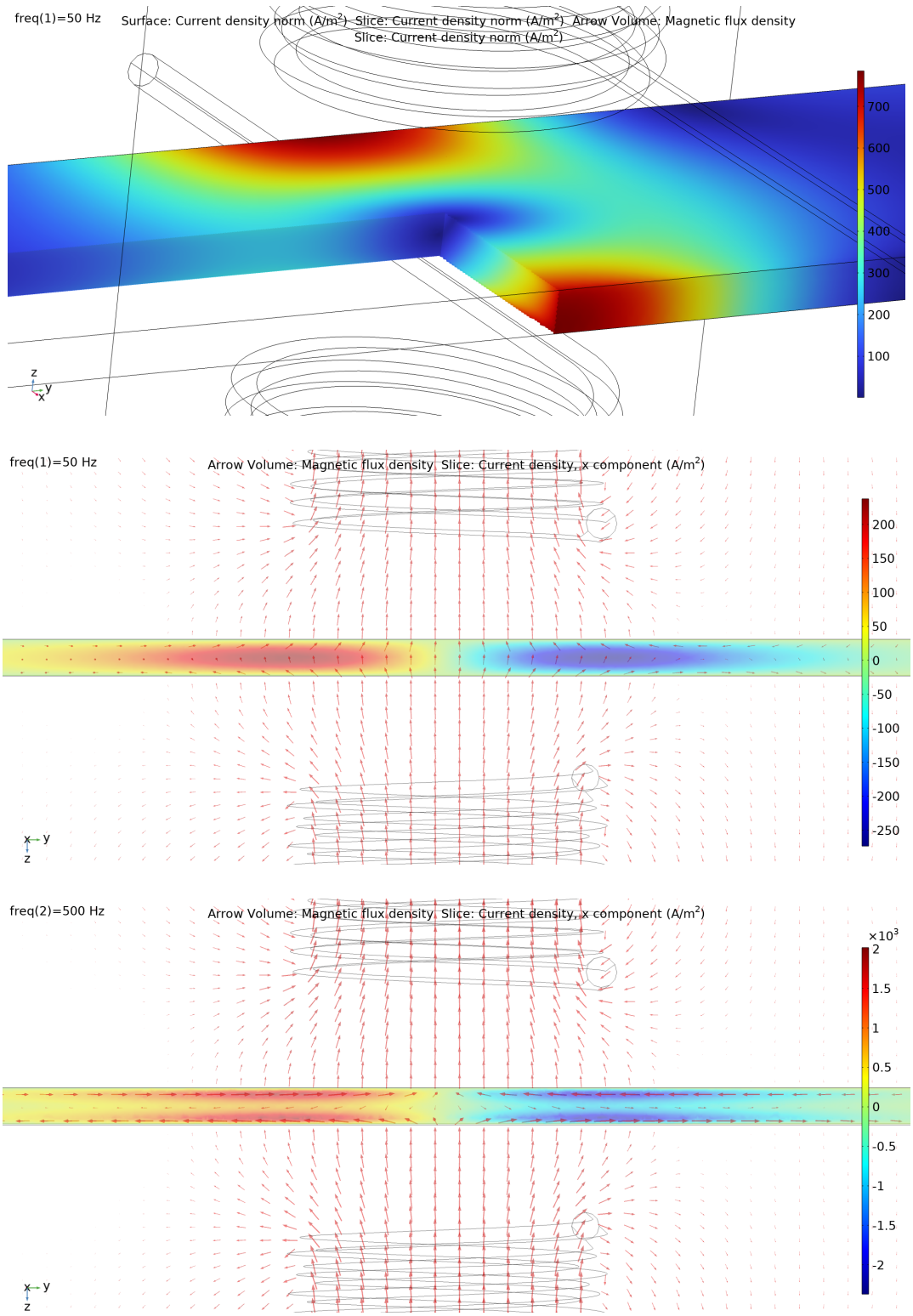

Figure 2.5: Visualization of eddy currents in an iron sheet, with 10A, 10 winding coils above and below. Colors indicate electric current density and arrows the magnetic flux density. Eddy currents can be seen to mainly flow in an annulus and weaken with penetration depth at higher frequency.

3 Sensor Theory

In this section the sensor output is modelled and several phenomena are discussed. For a detailed discussion of the sensor design, the input, output and data acquisition see appendix A.

3.1 Equivalent circuit of the sensor

As a model of the sensor an equivalent circuit can be used. An electronic circuit of the sensor can be seen in figure 3.1a. On the left side the circuit behind the transmitting coils is depicted. The transmitting coil is modelled as a transformer coupled with the receiving coil and the metal strip. The metal strip is included as a separate circuit on which the transformer e.m.f. acts and the resistor represents the eddy current losses. The circuit can be compacted by viewing the input to the transmitting coil as a current source and pulling the circuits behind the transformer through which requires appropriate scaling [13]. The compacted circuit is shown in figure 3.1b. This circuit would already be able to explain a large part of the typical EC sensor output as seen in A.3 [14]. The linear increase in gain is a result of the Lenz law dependence on the frequency which is implicit in an inductor. The initial 90° phase is also a result of this. When the strip is included, the resistor and inductor will at some frequency also start playing their effect, which causes the slower gain increase and the phase drop. The strong phase drop at high frequency is believed to be due to parasitic capacitance, without parasitic capacitance the phase would come back to 90° [14]. This parasitic capacitance could be included in the equivalent circuit as a shunt connection, with the appropriate damping to facilitate the gradual phase decrease (without damping the phase would flip practically instantly to −90°).

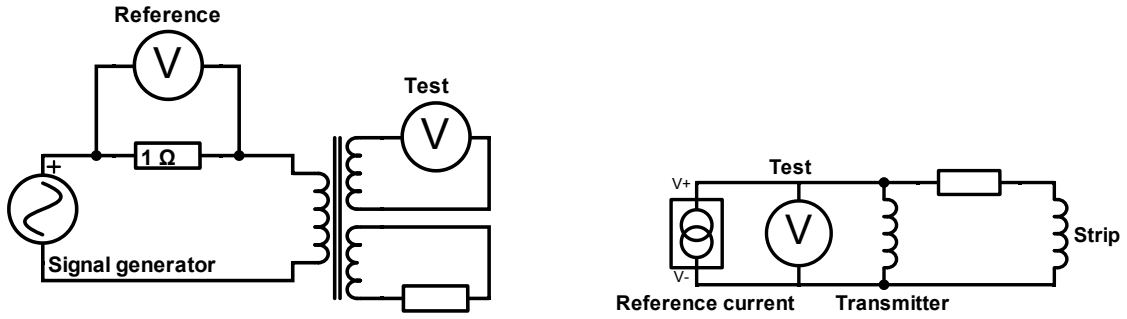

(a) Equivalent circuit of the sensor.

(b) Compacted equivalent circuit.

Figure 3.1: Transformer model of the sensor.

Although the equivalent circuit does explain the main effects of the sensor output, this simple model is not sufficient and does not fit the scope of understanding the sensor output and the relation with the microstructure. Firstly, the model does not give a quantitative relation between the components and the macroscopic physical quantities of permeability and

conductivity. Secondly, the components would need to be variable depending on frequency but also for example on the amount of material in the sensor as the inductance and eddy current loss change with those factors. Allowing for such dependence would either lead to over-fitting or require a physical-based model. Thirdly, if e.g. parasitic capacitance is to be included it is not clear which and where components should be included to represent physics correctly.

3.2 Magnetic circuits

3.2.1 Gyrator-capacitor model

To describe the variation of the sensor output due to the strip width and thickness we have to look at what is called the magnetic circuit. A magnetic circuit has close analogies with an electric circuit [9]. There are two prominent equivalent electronic models. For both, the electromotive force $\mathcal{E}$ corresponds to magnetomotive force (m.m.f.) $\mathcal{F}$. However, in one model current i corresponds to magnetic flux Φ, in the other model it corresponds to the time change of flux, $\dot{\Phi}$, also called the flux-rate [15]. Here the latter model, called the *Gyrator-Capacitor* model, will be used because of a few advantages like conserving energy relations. The bridge between the electrical domain and the magnetic domain, due to an inductor, is called a gyrator in this model, converting voltage to the flux-rate and current to m.m.f. as depicted in figure 3.2. The transmitter coil is the source of our m.m.f. and the change of flux is a source of voltage according to the relations:

$$\begin{aligned} \mathcal{F} &= Ni, \\ \dot{\Phi} &= v/N, \end{aligned} \tag{3.1}$$

with N the number of turns and v and i respectively the voltage and current through the coil. In this model, we have that the permeance $\mathcal{P}$ corresponds to capacitance, given by:

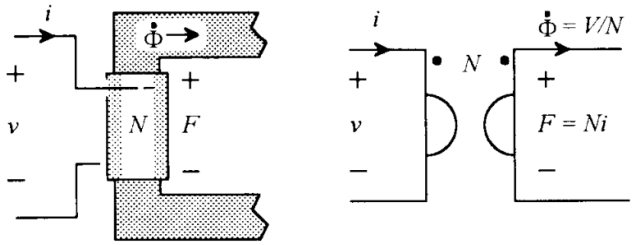

Figure 3.2: N-turn inductor modelled as a gyrator [15].

$$\dot{\Phi} = \mathcal{P}\frac{d\mathcal{F}}{dt} \tag{3.2}$$

$$\mathcal{P} = \frac{\mu A}{l} \tag{3.3}$$

with A the cross sectional area and l the length of the flux path. Flux paths are hence given by capacitors and losses by resistors. Here magnetic resistance will be denoted $\mathcal{R}$. Similar

to an electric circuit, these components can be brought together into magnetic impedance $\mathcal{Z}$:

$$\mathcal{Z} = \frac{\mathcal{F}}{\dot{\Phi}}. \tag{3.4}$$

As is maybe already observed, the gyrator looks a lot like an ideal transformer but it also takes the so-called *dual* of the impedance, swapping voltage and current. An impedance on the right side of figure 3.2 of $\mathcal{Z}$ is transformed to an impedance of $Z = N^2/\mathcal{Z}$ on the left side, where the gyrator has a scaling factor of N^2 with N called the gyration resistance.

3.2.2 Equivalent circuit of the magnetic field

During a measurement, the magnetic field lines are expected to follow the core without loss and pass through either the strip, where there might be some losses, or the air without loss. The 'voltage' source in the circuit is the m.m.f. $\mathcal{F}$ from the transmitter coil and we measure the 'current' $\dot{\Phi}$ with the receiver coil via Lenz' law. In figure 3.3 a quarter of the sensors circuit can be seen with $\mathcal{P}_\mathrm{a}$ the permeance of the air, $\mathcal{P}_\mathrm{s}$ the permeance of the strip, $\mathcal{P}_\mathrm{g}$ the permeance of the air gap between core and strip and $\mathcal{R}_\mathrm{s}$ the eddy current loss of the strip. It is assumed here that that all the flux generated by the transmitter coil is picked up by the receiver coil and that the permeance of the core is very large and hence can be ignored. For the permeance measurements, the flux will not be able to pass straight through to the other m-shaped core. In the eddy current mode this option will be available, in addition to the path along the length of the strip.[4] In the figure the component names for this secondary path are appended with a 2. For the permeance measurements the magnetic impedance will be:

$$\mathcal{Z}_\mathrm{P} = \frac{1}{j\omega\mathcal{P}_\mathrm{a} + \dfrac{1}{\dfrac{1}{j\omega\mathcal{P}_\mathrm{s}} + \dfrac{1}{j\omega\mathcal{P}_\mathrm{g}} + \mathcal{R}_\mathrm{s}}}, \tag{3.5}$$

where j is the imaginary unit, and ω the radial frequency of the m.m.f. source. As might have been noticed, the equivalent circuit of the magnetic field is closely connected with the equivalent circuit of the sensor from section 3.1. In a sense the inductance of the coils is modelled. This also means that this model suffers some of the same problems. The relation with the permeability is a bit more concrete but the eddy current power loss is still simply a resistance without clear origin for it's magnitude and parasitic capacitance is also not in the model. Additionally, in the general case the permeability and eddy current depend on frequency and amplitude. For this model we take the permeability to be constant. The resistance is more complicated but the eddy current component should have a constant resistance in this model [16].

[4] In conventional electrical circuits this path should cancel out, however here it doesn't, see for example figure 2.5. This effect has been separately found by Wiard van der Weijden in an extensive finite element model of this sensor.

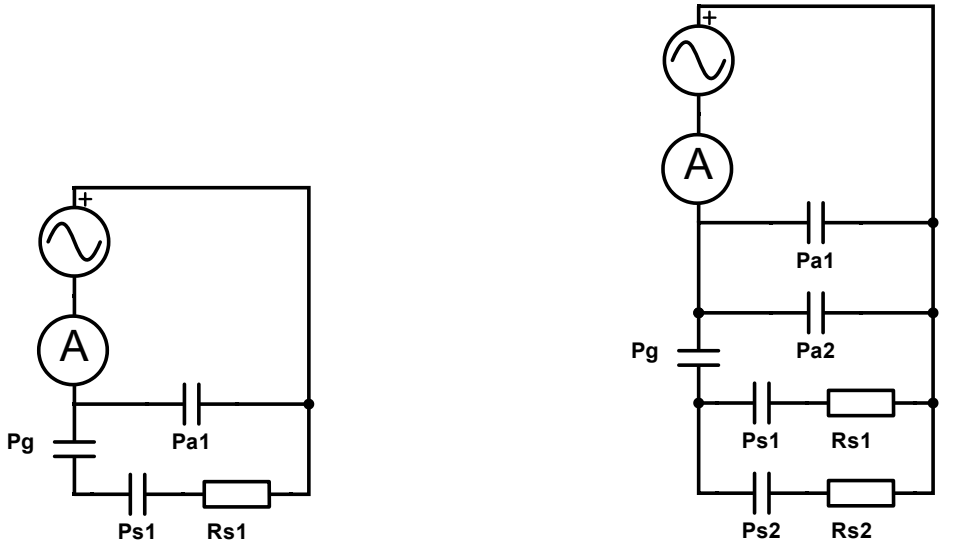

(a) Permeance mode circuit.

(b) Eddy current mode circuit.

Figure 3.3: Gyrator capacitor model of the sensor.

3.2.3 Width and thickness dependence of permeance mode

Since the strip is relatively thin with respect to the rest of the sensor, it is assumed that the permeance through air is not affected by the amount of material in the sensor. Measuring the difference in gain with and without strip should then give a good indication of the permeance through the strip and the air. These values will be taken from the low frequency regime to minimize distortions due to the eddy currents and parasitic capacitance, which means the resistance can be ignored.

Since we measure voltages, we would like to translate the magnetomotive force and the change of flux to voltages. Using relations (3.1) and $v_{\text{ref}} = i_{\text{ref}}R$, with $R = 1\,\Omega$ and i_{ref} the current through the transmitting coil, we can write:

$$\frac{v_{\text{test}}}{v_{\text{ref}}} = \frac{2N_{\text{test}}\dot{\Phi}}{\mathcal{F}/2N_{\text{ref}}} = \frac{1960}{\mathcal{Z}_{\text{full}}} = \frac{1960}{\mathcal{Z}_{\text{quarter}}/2}, \tag{3.6}$$

where v_{test} and v_{ref} are the test and reference voltages respectively and $N_{\text{test}} = 14$ and $N_{\text{ref}} = 35$ the number of windings of the respective coils. We have $\mathcal{Z}_{full} = \mathcal{Z}_{half} = \mathcal{Z}_{quarter}/2$ as the impedance of the full circuit will be equal to that of only a single core as the model is symmetrical and the flux paths are separated which will in turn be double the impedance of a quarter of the core. To be able to model the effect of thickness and width we need to employ (3.3), in which the height of the air gap depends on the thickness of the strip as

follows:

$$\mathcal{P}_\mathrm{s} = \frac{\mu_\mathrm{s} w t}{2l}, \tag{3.7}$$

$$\mathcal{P}_\mathrm{g} = \frac{2\mu_\mathrm{g} w t_\mathrm{g}}{2(h-t)}, \tag{3.8}$$

with μ_s and μ_g the permeabilities of the strip and air gap respectively, w the width of the strip, t and t_g the thickness of the strip and gap respectively and h the height of the air gap without strip. The factors 2 are included because only a quarter of the sensor is taken here and hence only half the thickness should be taken. For the gap there is an extra factor two since there are two air gaps of the same size: in the middle and the side. Note that because the air gap is only variable on one side the problem is not strictly symmetrical but this asymmetry can be absorbed in the unknown constants. Using these relations we can write the equation for the P mode in the low frequency regime as:

$$\begin{aligned}
\frac{v_\mathrm{test}}{v_\mathrm{ref}} &\propto j\omega\mathcal{P}_\mathrm{a} + j\omega\frac{\mathcal{P}_\mathrm{s}}{\mathcal{P}_\mathrm{s}/\mathcal{P}_\mathrm{g}+1} \\
&= j\omega\left(\mathcal{P}_\mathrm{a} + \frac{\frac{\mu_\mathrm{s}}{2l}wt}{\frac{\mu_\mathrm{s}}{2\mu_\mathrm{g} l t_\mathrm{g}}t(h-t)+1}\right) \\
&\approx j\omega\left(\mathcal{P}_\mathrm{a} + \frac{\mu_\mathrm{s}}{2l}wt - \frac{\mu_\mathrm{s}^2 h}{4\mu_\mathrm{g} l^2 t_\mathrm{g}}wt^2\right).
\end{aligned} \tag{3.9}$$

In the last step a Taylor expansion around $t = 0$ is taken for fitting purposes. Note that the first order term is the permeance of the strip, the second order term is a correction taking the gap into account. Rewriting the equations to obtain the exact coefficients with least squares is possible but it was found that the fit would not give significant results for all the coefficients.

A theoretical relation with thickness and width can be obtained when some of the unknown values are guessed. Taking

$$\mathcal{P}_\mathrm{a} = \frac{\mu_\mathrm{a} w_\mathrm{a} t_\mathrm{a}}{2l}, \tag{3.10}$$

with $\mu_\mathrm{a} = \mu_\mathrm{g} = \mu_0$, $\mu_\mathrm{s} \approx 47\mu_0$, $w_\mathrm{a} \approx 0.05\,\mathrm{m}$ the width of the core, $t_\mathrm{a} \approx 0.002\,\mathrm{m}$ the height of the air gap, $t_\mathrm{g} \approx 0.0075\,\mathrm{m}$ the width of the air gap, $l \approx 0.01\,\mathrm{m}$ and $h \approx 0.001\,\mathrm{m}$ gives:

$$\left|\frac{v_\mathrm{test}}{v_\mathrm{ref}}\right| \approx 1.55 \cdot 10^{-4} f + 72.7 f w t - 2.28 \cdot 10^4 f w t^2. \tag{3.11}$$

From this we can see that with a thickness of around 0.2 mm, the correction term is in the order of 10% of the first order term. At high frequency the resistance can no longer be ignored and the gain becomes more difficult to express in an insightful manner and won't be given here. However, the high frequency regime is easy to express and is given by:

$$\left|\frac{v_\mathrm{test}}{v_\mathrm{ref}}\right| = \omega\mathcal{P}_\mathrm{a}, \tag{3.12}$$

since the resistance limits the flux-rate through the strip path at higher frequency. Note that this does not account for the parasitic capacitance. An attempt has been made to model this parasitic capacitance however due to time constraints and uncertainty in the damping terms this was not finished. Furthermore, various attempts have been made to model the EC mode as well but these were not successful. Hence mostly only phenomenological effects will be looked at.

3.2.4 Phase predictions

For the phase we can also write down a formula, but since the interesting features occur at higher frequency where the capacitive effects influence the results, it is not useful for fitting purposes nor is such long formula very insightful. To condense the information, the critical frequency ω_c and phase $\phi(\omega_c)$ at which the characteristic phase minimum occurs will be looked at. Solving for the minimum gives:

$$\omega_c = \frac{\sqrt{\mathcal{P}_a(\mathcal{P}_g + \mathcal{P}_s)(\mathcal{P}_a\mathcal{P}_g + \mathcal{P}_a\mathcal{P}_s + \mathcal{P}_g\mathcal{P}_s)}}{\mathcal{P}_a\mathcal{P}_s\mathcal{P}_g\mathcal{R}_s} \tag{3.13}$$

$$\begin{aligned}\phi(\omega_c) &= \arctan\left(\frac{2\sqrt{\mathcal{P}_a(\mathcal{P}_g + \mathcal{P}_s)(\mathcal{P}_a\mathcal{P}_g + \mathcal{P}_a\mathcal{P}_s + \mathcal{P}_g\mathcal{P}_s)}}{\mathcal{P}_s\mathcal{P}_g}\right) \\ &= \arctan\left(2\mathcal{P}_a\mathcal{R}_s\omega_c\right)\end{aligned} \tag{3.14}$$

From these equations we expect that if the width of the strip is decreased, which causes a decrease in $\mathcal{P}_s$ and $\mathcal{P}_g$, that the critical frequency increases hence also the phase minimum increases. Increasing the thickness would increase $\mathcal{P}_s$ and $\mathcal{P}_g$. This then decreases ω_c and lowers the phase minima. There could possibly be a change in $\mathcal{R}_s$, altering the critical frequency.

To predict the phase change for the eddy current mode the same procedure can be followed. To make things easier the paths from the permeance mode will be omitted due to them being minor in comparison. Therefore, the same equations can be used for the investigation. The strip permeance $\mathcal{P}_s$ in this case is much larger than the gap permeance $\mathcal{P}_g$, as the secondary path through the strip is very short and the permeability factors higher, the critical frequency can be simplified further as:

$$\omega_c \approx \frac{\sqrt{\mathcal{P}_a(\mathcal{P}_a + \mathcal{P}_g)}}{\mathcal{P}_a\mathcal{P}_g\mathcal{R}_s}. \tag{3.15}$$

In case of increasing thickness this would mean increasing $\mathcal{P}_g$. With this we can predict ω_c to go down and hence the phase as well.

In this case decreasing the width would also mean decreasing $\mathcal{P}_g$ but now it would also mean additionally increasing $\mathcal{P}_a$. Since the values involved here are in the same order of magnitude, the effect this has depends on the width in question. Because of the approximations used, it is difficult to say what the real effect is. If we assume the change in width causes an equal change in permeance for both the air and the gap then we have $\Delta\mathcal{P}_a + \Delta\mathcal{P}_g = 0$, with $\Delta\mathcal{P}$ indicating the difference in permeance due to the change in width. This would give ω_c to stay the same, with the phase going up due to increasing $\mathcal{P}_a$.

4 Material characterization

The material of research is AISI 420, a martensitic stainless steel. The nominal composition in percentages is: C 0.32, Si 0.2, Mn 0.3, P $\leq$ 0.025, S $\leq$ 0.010, Cr 13.7, with the remaining material Fe. [17] Due to the chromium it is called a stainless steel, meaning the material is corrosive resistant. It is called martensitic because the material becomes dominantly martensitic when hardened by heating to high temperatures. However, in the annealed state the material matrix is solely in ferritic phase. The material contains a large amount of precipitates in the form on chromium carbides, as can be seen in figure 4.1. These carbides give the material a better wear resistance due to their high hardness. The material in question is rolled to thin sheets of 0.2 mm thickness, although other thicknesses are also available. The material used in this report is as delivered, which is in an annealed state as can be seen in figure 4.2a.

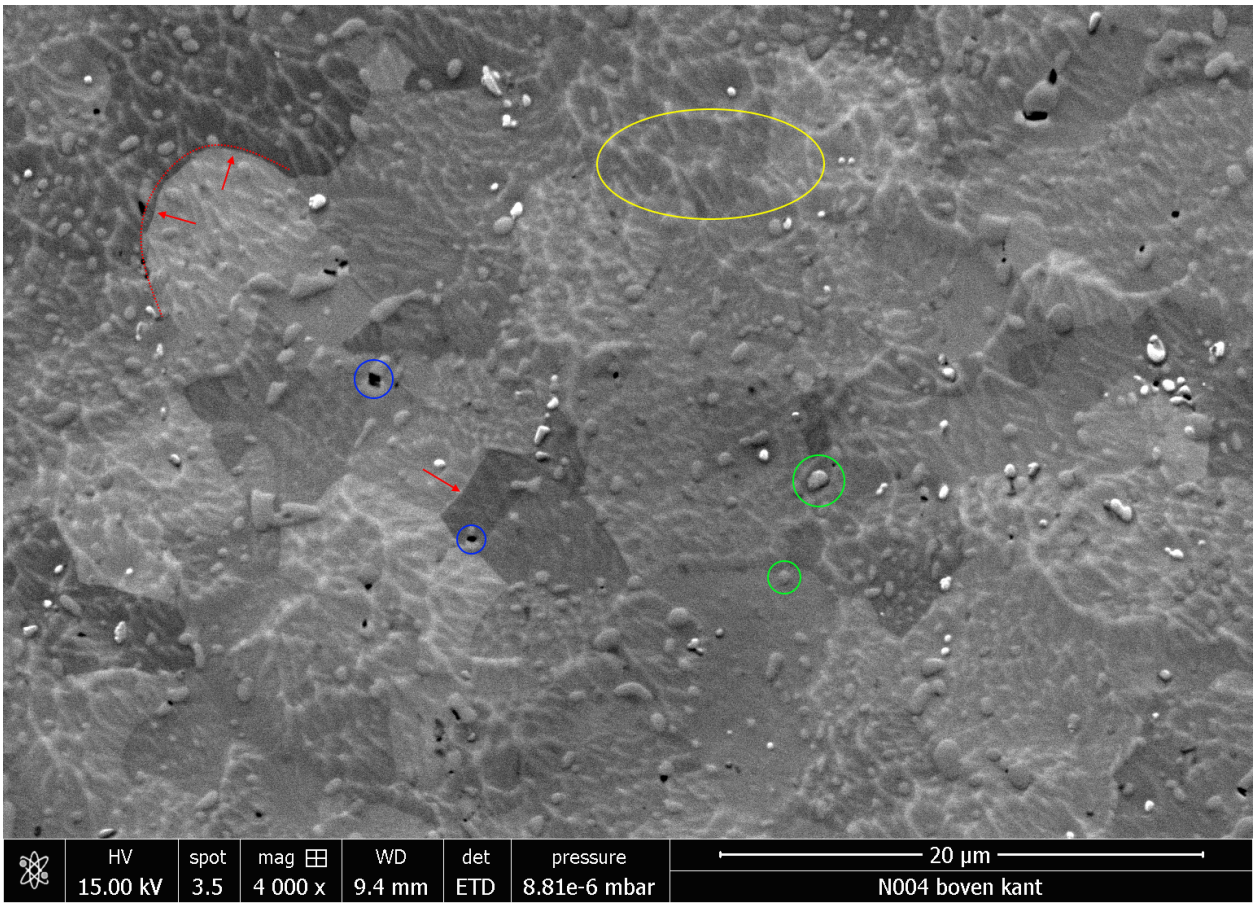

Figure 4.1: SEM picture of AISI 420. The green highlights some carbides, the blue encircling shows holes which housed carbides and red marking indicates grains boundaries. The yellow encompasses dendritic, wave-like patterns which might be due to over-polishing [18].

Strips were strained until 1%, 3%, 5%, 7.5% and 10% engineering strain and then released. Each strip width was measured with vernier calliper and the thickness with a micrometer.

The relative change in width and thickness is plotted in figure 4.2b. Fitting the curves obtained gives the following relations:

$$w = 37.95(2) - 21.4(3)\varepsilon, \tag{4.1}$$

$$t = 0.1983(4) - 0.058(7)\varepsilon, \tag{4.2}$$

with w and t the width and thickness respectively and ε the engineering strain in the length. These relations have R-squared values of 0.9992 and 0.9445 respectively. A different, prior experiment with measurement of the width during tensile testing on AISI 420 also showed that the strain in the length and width has an approximately linear relation, even during elastic deformation. These relations show that a deformation in the length causes an opposite deformation of that of around 55% in the width and around 30% in the thickness. This matches well with an r-value or *Lankford coefficient*, of around 1.8 found from volume invariance.

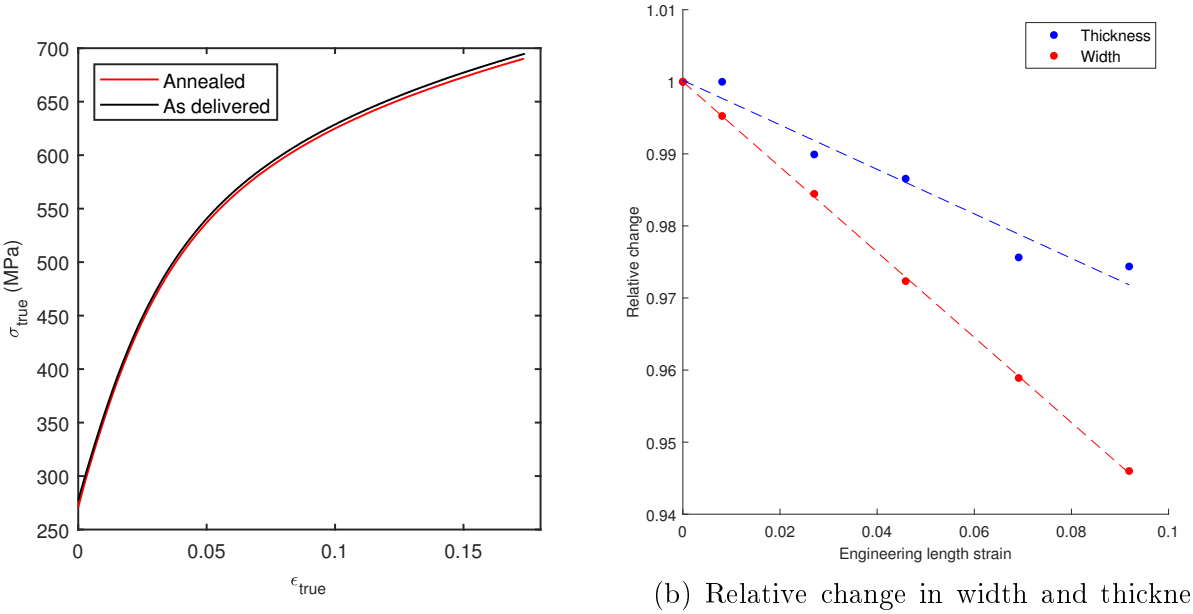

(a) Stress-strain curve of AISI 420.

(b) Relative change in width and thickness due to length strain.

Figure 4.2: Tensile properties of AISI 420.

5 Experimental Methods

5.1 Tensioning

For the in-situ measurements, the sensor was mounted in an automated tensile bench, where some care has been taken that the tensioned strip would sit straight in the middle of the sensor. Because the strip was not tensioned until breaking, no tensile bar with a waist region had to be used. Cyclic elongation of the specimen was opted for to give information on both unloaded and loaded states for various strains. The strip was deformed in steps of 1% engineering strain. At each step the strain was held for five seconds, before unloaded to some small prestress, where is was also held for five seconds after which next next cycle started. The sensor measured every second. Figure 5.1 shows the sensor in the tensile bench.

For the ex-situ measurements the strip was simply tensioned until the desired strain and then released, after which various measurements could be performed.

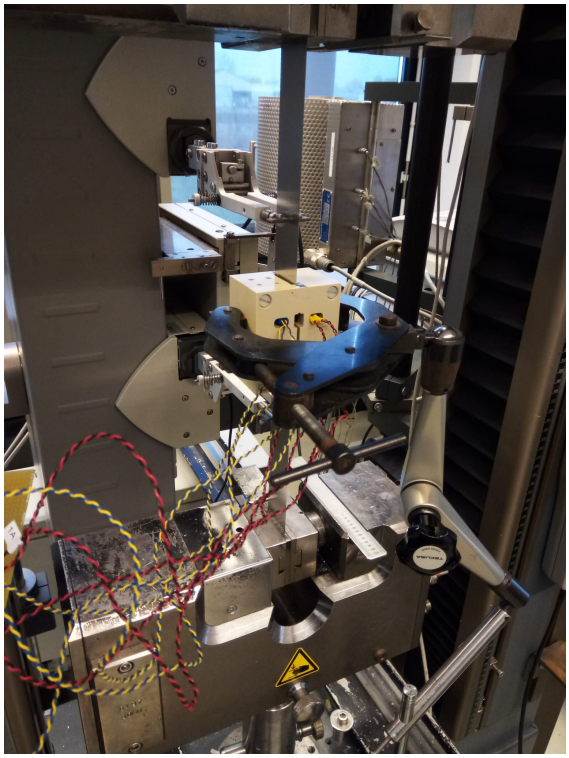

Figure 5.1: Tensile bench with sensor.

5.2 Resistivity

Using the 4-point probes method the resistivity was measured. The voltage probes were embedded in a stiff insulator with a fixed distance of around 25 cm apart and the strip to be measured was aligned to the side of the insulator, ensuring that the distance over which the voltage is measured is constant across measurements. The voltage probes were connected to the DAQ card, which had around 0.2 mV accuracy. The current was measured with a multimeter. See figure 5.2 and 5.3 for the setup.

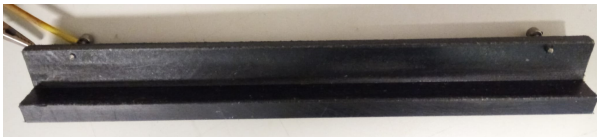

Figure 5.2: Embedded voltage probes.

Figure 5.3: Measurement of resistivity.

5.3 Permeability

To measure the magnetic properties like permeability a VSM was employed. Samples for the VSM were made by cutting a square of 8 by 8 mm from each elongated strip using a Synova laser cutter to minimize residual stresses from cutting. The sample was stuck to a glass holder using some tape which was put into the VSM seen in figure 5.4.

Another method to find the permeability was employed, which used the inductance of a coil around a stack of coated sheets, see figure 5.5. The inductance was modelled for various sheet permeabilities and compared to measurements to find the actual strip permeability.

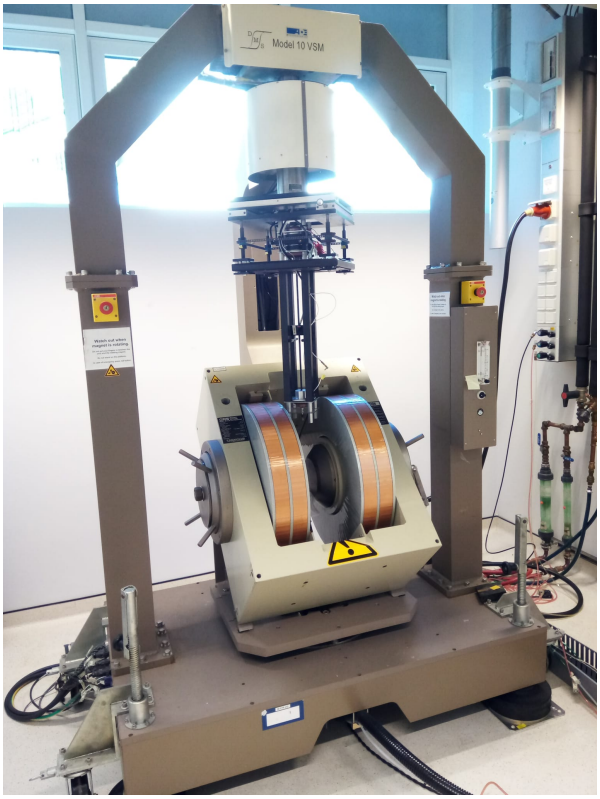

Figure 5.4: VSM 10.

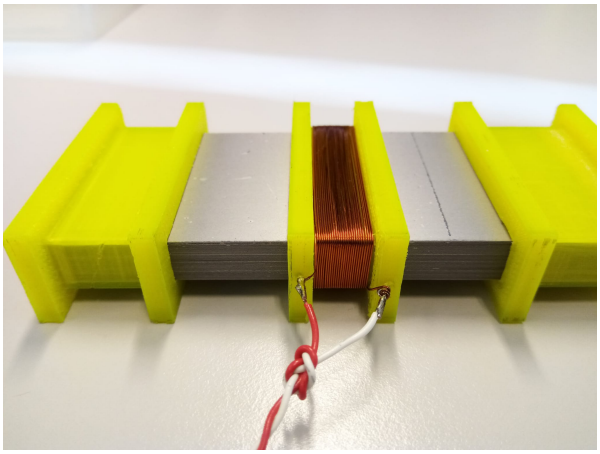

Figure 5.5: Measurement of permeability using inductance.

5.4 EBSD

The first step in analysing the microstructure of the material was looking at the grain sizes and orientations. For this electron back scatter diffraction (EBSD) was employed. The sample was mounted in 'MultiFast Red', a bakelite hot mounting resin from Struers. The criteria used to classify a grain with the OIM Analysis v8.0 software was a tolerance angle of 1°, 25 points per grain and requiring multiple rows per grain. Before analysis grain dilation with these settings was applied twice to de-noise the data. To get a measure of the dislocation density the default 'first nearest neighbour' setting for the kernel average misorientation (KAM) was applied.

5.5 MFM

Various attempts have been made to visualize the domains in the samples, with as eventual goal to compare domain configurations different pre-strains. Probably the nicest images can come from Kerr imaging [19]. An attempt was made to do this but the material was most likely not well polished enough. Successful MFM pictures were obtained with an Cypher S AFM with a MESP-V2 CoCr coated cantilever on interleave mode. The cantilever was magnetized perpendicular to the sample by placing it in a holder with integrated magnet for 10 minutes. The material was polished with OP-S with $\leq 0.25\,\mu m$ colloidal silica using the same mounting resin as before. To fit in the AFM the sample was removed from the mount by breaking the mount in two.

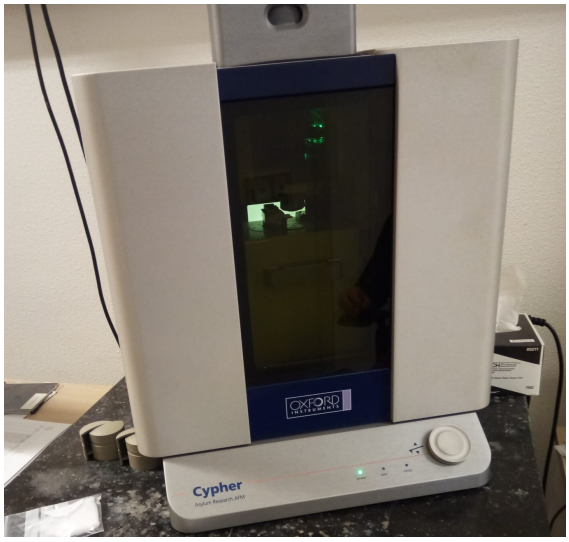

Figure 5.6: AFM for MFM measurements.

The phase of the cantilever yields the magnetic information as the natural frequency of the cantilever is altered due to the magnetic field from the sample interacting with the tip. More specifically, the phase θ between the driving frequency ω_d and the cantilever resonant

frequency ω_r is given by: [20]

$$\theta = \arctan\left(\frac{\omega_r \omega_d}{Q(\omega_r^2 - \omega_d^2)}\right), \tag{5.1}$$

$$\omega_\mathrm{r} = \omega_\mathrm{n}\sqrt{1 - \frac{1}{k}\frac{\partial F_z}{\partial z}} \approx \omega_\mathrm{n}\left(1 - \frac{1}{2k}\frac{\partial F_z}{\partial z}\right), \tag{5.2}$$

with the natural frequency ω_n, quality factor Q and spring constant k of the cantilever, and F_z the force in the z direction, which is taken to be perpendicular to the sample. This force can be given in terms of the magnetic field H and volume and surface charge densities ρ and σ as:

$$F_z = \iiint_\mathrm{sam} \rho_\mathrm{sam} H_{\mathrm{tip},z} + \iint_\mathrm{sam} \sigma_\mathrm{sam} H_{\mathrm{tip},z} \tag{5.3}$$

$$= \iiint_\mathrm{tip} \rho_\mathrm{tip} H_{\mathrm{sam},z} + \iint_\mathrm{tip} \sigma_\mathrm{tip} H_{\mathrm{sam},z}. \tag{5.4}$$

Here the subscripts 'sam' and 'tip' indicate the field and magnetic charges due to the sample and tip respectively. The phase is hence a measure of a change in charge density, which we expect to be near a wall. Not all walls have the same effect however, as Bloch walls only have surface charges for example, while Néel walls also have volume charges [8, 9, 20]. Moreover, at a tip height comparable or larger than the domain width the wall contrast vanishes and mainly a domain-like contrast remains [20].

6 Results & Discussion

Most of the processing steps that can be done on the material like tensioning and cold rolling, which we would like to use to understand the sensor output better, change multiple parameters simultaneously. Rolling and tension induce anisotropy in the material, increase the dislocation density and the width and decrease the thickness. A different processing step proposed was bending the material back and forth. This method would in principle not change the material dimensions. A few attempts were made with a manual rolling mill but it was quickly found out that manual variations and the repeated bending did not lead to a straight strip. The local wobbles caused high variation in sensor output, despite the strip guidance. Because of these complications, this processing step was abandoned and attention was focussed on tensioning the strip due to it being readily available and the possibility of measurement during tensioning (in-situ). To separate the effects, first the influence of thickness and width needed to be investigated. In section 3.2.2 a relation between the sensor output and the material parameters has been modelled. The validity of this model has to be established. Moreover, due to unknown parameters such as the actual path length of the flux through the strip or the amount of leakage flux, a quantitative relation can not be established based on the model alone.

6.1 Dimensional dependence

To find a relation with thickness and the width, strips of 0.20, 0.35 and 0.50 mm thickness were measured and reduced in width before being measured again. Due to the strip guidance being only on the side, the strip was aligned up to the side of the sensor to ensure the same height is kept throughout the process. The widths evaluated were approximately 15, 20, 25, 30, 35 and 38 mm. Due to manual cutting, the width of the strips were often not exactly these values, nor were they the same width everywhere. Therefore the width has been measured right in front of the sensor and right behind the sensor with a vernier calliper. For fitting purposes the average of the two values has been taken. A part of the sensor output in the P mode can be seen in figure 6.1, where the inductance and the phase are plotted against frequency. As can already be seen from the figure, at low frequency, around up to 2000 Hz the inductance is more or less constant with increasing gain for higher width and thickness. The phase drop occurs at lower frequency for thicker material, as is to be expected as the eddy currents are more prominent the higher the thickness. Whether this also decreases the phase minima is not clear due to the effects of parasitic capacitance overlapping. Decreasing the width does indeed lower the phase minima but it does not seem to decrease the frequency, although this is also not clear. From the inductance plot it is also visible that the gain for thicker strips eventually drops below that of the thinner strips, indicating also that thinner material is less affected by eddy currents at the same frequency. At high frequency the distinction between thicknesses blurs again and the width seems to be the dominant effect.

6.1.1 Fitting low frequency permeance mode

To fit the data, first the slope of the gain versus the frequency is found from the reference input. This will yield the first part of (3.9), that is: $7840\pi\mathcal{P}_\mathrm{a}$. Using this, the data can be

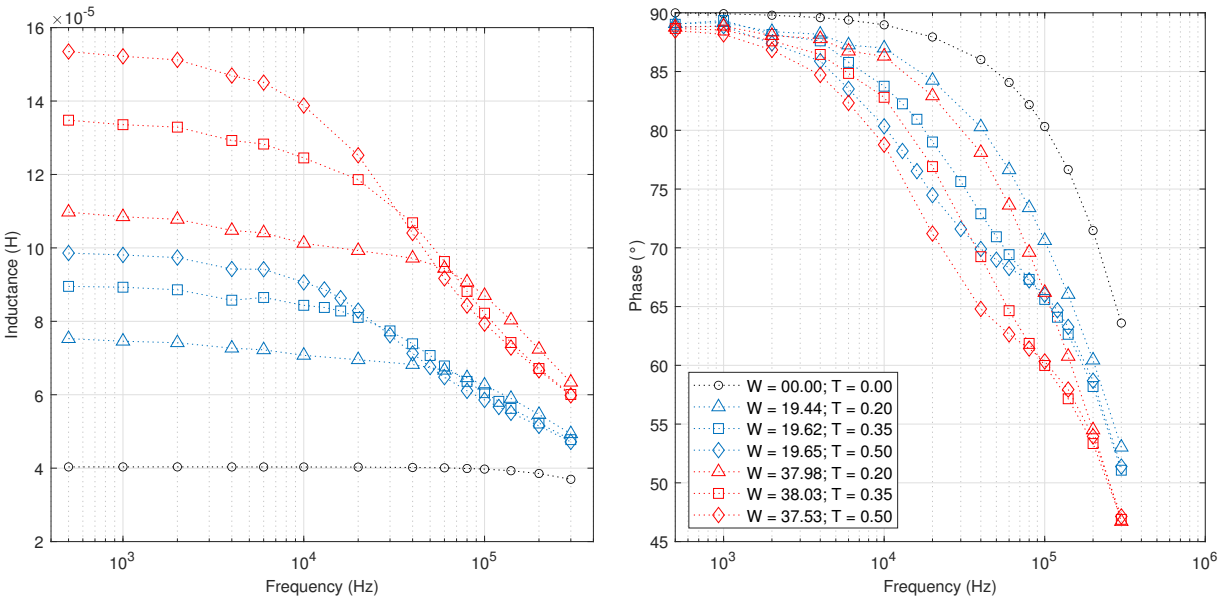

Figure 6.1: P mode inductance (left) and phase (right) versus frequency for various widths and thicknesses.

fitted with the former result as intercept of the curve. R was used to obtain a linear model, of which the code can be found in appendix B. The fitted model up to 2000 Hz was:

$$\left|\frac{v_{test}}{v_{ref}}\right| = 2.5353(2)\cdot 10^{-4} f + 6.98(9)\cdot 10^{1} fwt - 6.45(19)\cdot 10^{4} fwt^2, \tag{6.1}$$

with w and t the width and thickness respectively in m and f the frequency is Hz. The model has highly significant p values of $p < 0.001$ and an adjusted R-squared of 0.998. The most significant outlier is the data point with highest frequency, thickness and width. It has a Cooks distance of over 0.5 and is reasonably influential. The Bonferroni p value also flags this outlier as significant with $p = 0.002$. All the points flagged as influential are from 2000 Hz, indicating a slight deviation from the linear relation with frequency which can also be seen from the inductance graph in figure 6.1 not being exactly horizontal. To account for this slight difference also a model for specifically 500 Hz has been fitted which comes very close to the larger model but is less suited for other frequencies:

$$\left|\frac{v_{\mathrm{test}}}{v_{\mathrm{ref}}}\right|_{f=500} = 1.2677(1)\cdot 10^{-1} + 3.58(8)\cdot 10^{4} wt - 3.35(19)\cdot 10^{7} wt^2. \tag{6.2}$$

Here too, the model is highly significant with $p < 0.001$, has an adjusted R-squared of 0.998 and from the diagnostics plot in figure 6.3 we can see that the model fitted has residuals close around zero and data that is close to normality. The residuals do show a trend with a peak in the middle, giving the suggestion that the data deviates from linearity. This should not come as a surprise since the flux paths are not necessarily straight. In this case however, the outlier test indicates that the outlier is not significant with Bonferroni p value of $p = 0.199$. The various data points and the fit can be seen in figure 6.2a where the gain is plotted against the width.

Comparing (6.2) with (3.11) shows that the fitted values are close to the guessed values. The best match is the second coefficient and the worst the third coefficient with factor three. Because an extra approximation was made with the Taylor expansion, it is understandable that this value has the largest offset. The quadratic thickness dependence is shown in figure 6.2b. The quadratic fit looks okay but can almost surely not be extrapolated to higher thickness as the gain is not expected to decrease. Instead, a linear relation could also be correct, if the zero width is not taken into account.

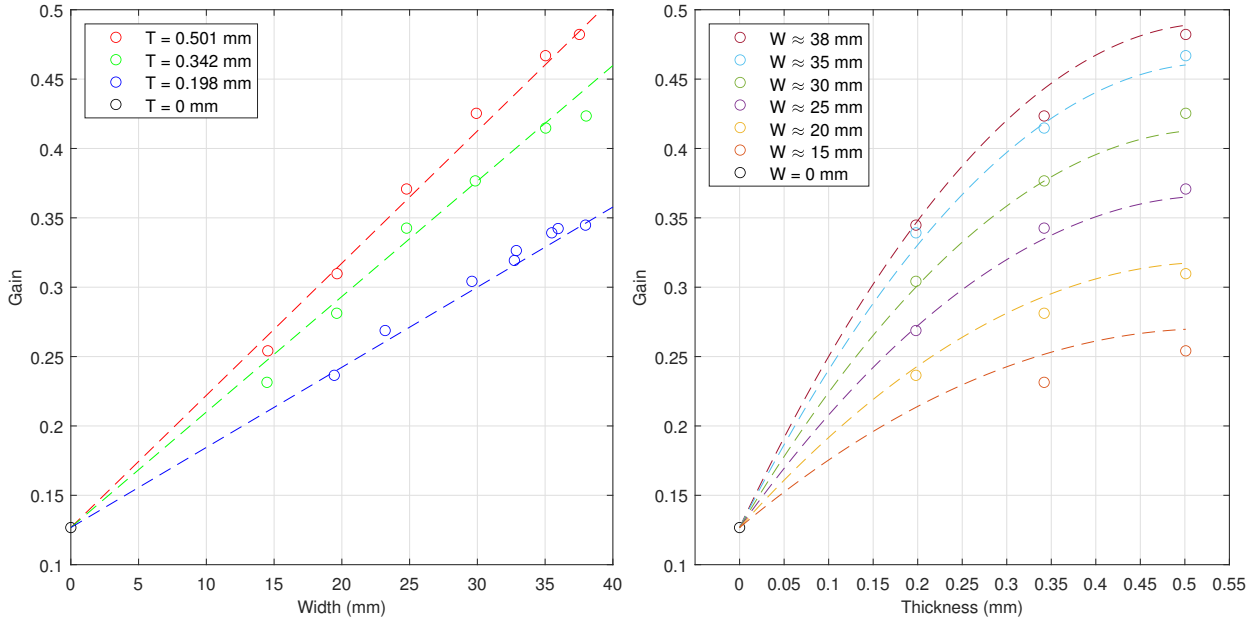

(a) Various thicknesses (T).

(b) Various widths (W).

Figure 6.2: Fit of the model at $f = 500\,\mathrm{Hz}$.

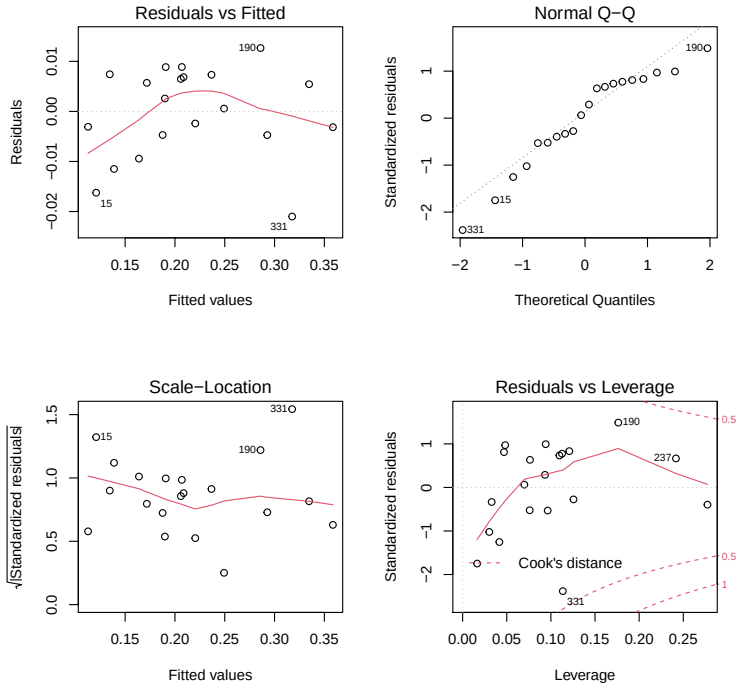

Figure 6.3: Diagnostics plot of the model at 500 Hz.

6.1.2 Eddy current mode phenomena

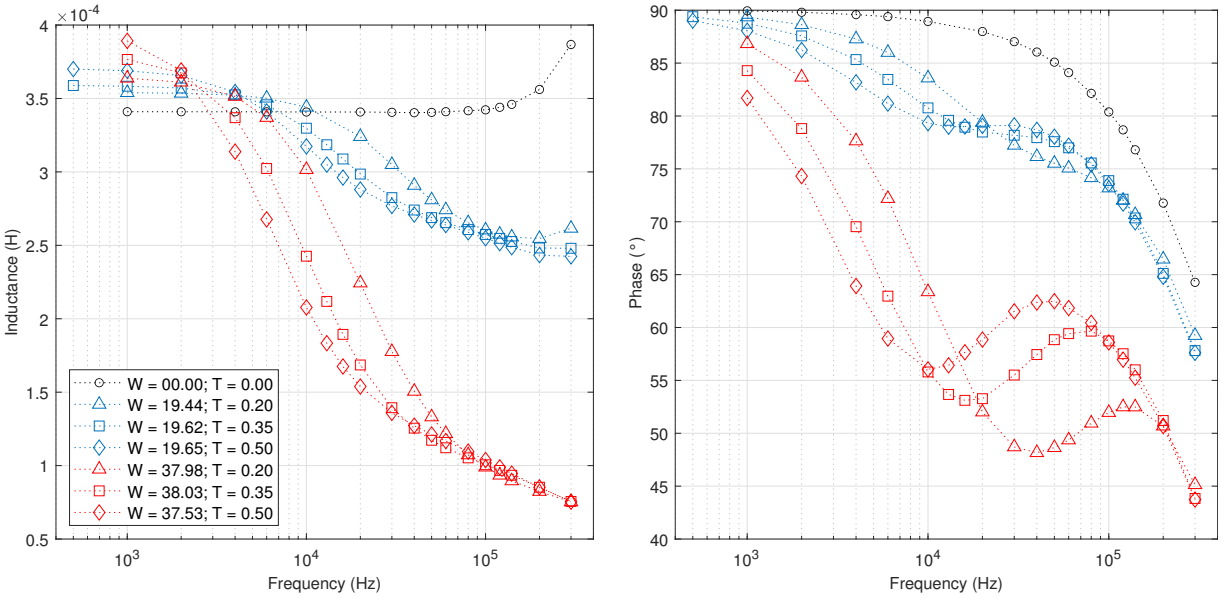

Figure 6.4: EC mode inductance (left) and phase (right) versus frequency for various widths (W) and thicknesses (T).

A part of the EC mode measurements for various widths and thicknesses can be seen in figure 6.4. Like the P mode the inductance increases at low frequency with the width and thickness, although the increase is a little lower in comparison, likely because of the secondary air path. At higher frequency we can see that the thinner strips have higher inductance, similar to the P mode. Here the effect of width is much more pronounced as the widths of similar size are all grouped together. This should be expected as the secondary air path is influenced strongly by the width of the strip. The phase shows, as in the P mode case, a lower critical frequency for higher thickness. Here the phase minimum does go up clearly for higher thickness, in contrast to the model. At least part of this can be explained by the parasitic effects being smaller at lower frequency, how much can be attributed to this is unclear. Using a spline to find the lowest points shows the critical frequency does not have a clear increasing or decreasing relation with the width, as expected.

6.2 Pre-strained specimen

6.2.1 Permeance mode

The sensor data from the pre-strained P measurements can be seen in figure 6.5. To account for the width and thickness change due to elongation, the relation 6.2 can be used. The difference between the predicted value of a strip with elongation and without elongation is taken to find the signal reduction due to the deformation. This value is subsequently added to the gain to find the deformation corrected response. The result of this can be seen in figure 6.6. From the figure it can be seen that the gain quickly drops from 0% to 1% elongation and becomes more or less constant for higher strains when the deformation is corrected for. Since it is believed there are no other factors with a large effect on the permeance apart from permeability, it is suspected that the permeability changes in roughly the same way.

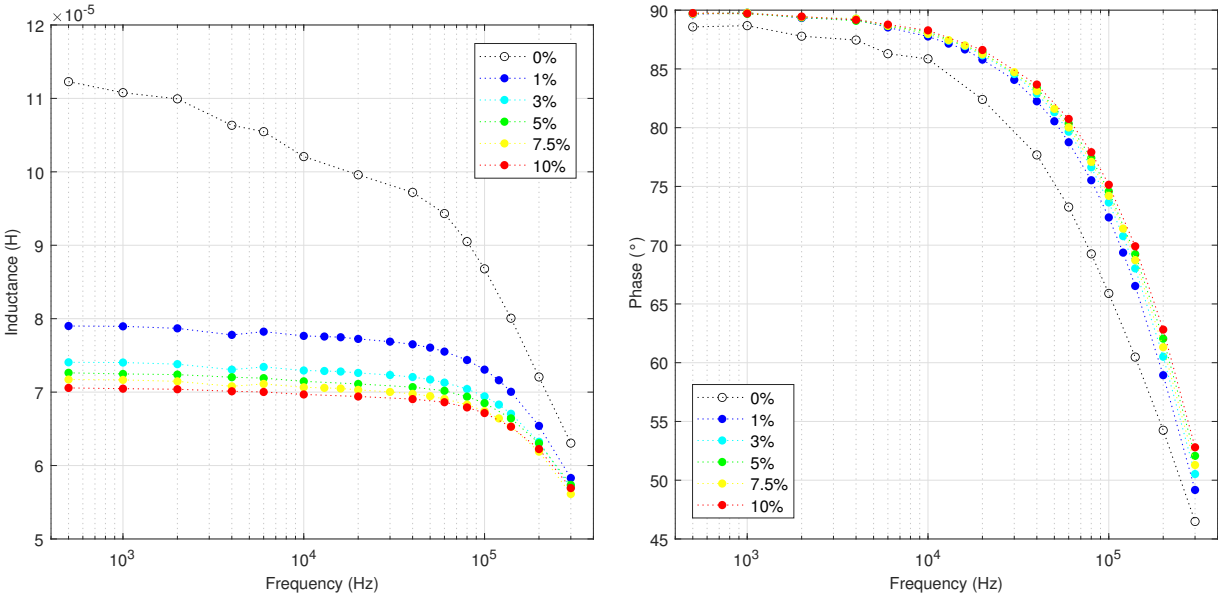

Figure 6.5: P mode inductance (left) and phase (right) versus frequency for various elongations.

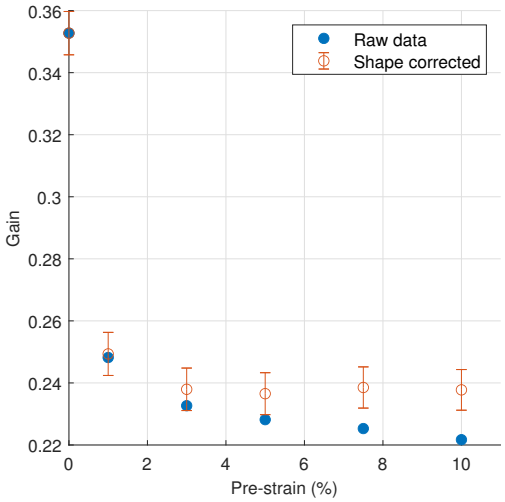

Figure 6.6: Gain and its deformation corrected value for various elongations at $f = 500\,\mathrm{Hz}$. Error bars indicate the 95% confidence interval.

6.2.2 Resistivity

To understand the EC mode, the resistivity of the material is also important. The measurement results can be found in figure 6.7. To obtain the resistivity the values from the figure have to be divided by around 0.25 to get a resistivity of around $49.7(5)\,\mu\Omega\,\mathrm{m}$ in the unstrained state. The error bars indicate the measurement reading errors and are mostly due to the uncertainty in the thickness. The 3% strain sample has a deviation during a measurement, possibly due to inconsistent and or diagonal placement of the voltage probe with respect to the strip due to manual variations or due to sagging of the strip. It should be noted that the strips were measured after a small specimen was extracted, as can be seen in figure 5.3. The hole could have had a slight influence on the homogeneity of the current along the strip. From the plot can be seen that the resistivity does not change to a large degree, at worst around 2%. The inductance however does drop strongly with pre-strained specimen and hence is not expected to depend on the resistivity.

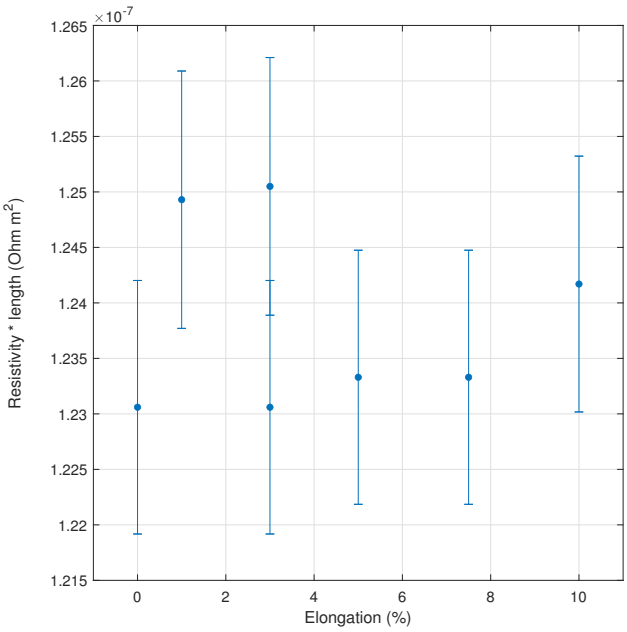

Figure 6.7: Resistivity times the probe distance versus elongation.

6.2.3 Eddy current mode

Since the inductances of the EC mode did not show a clear distinction, only the phase is looked at. As before, the phase minima will be looked at using a spline fit. In figure 6.8 the phase minima and the critical frequency are shown. A clear monotone increase with elongation is visible for the critical frequency, as is expected due to the decrease of width, thickness and permeability. The phase minimum does decrease strongly from 0% to 1% but fluctuates for the higher elongations. This indicates that the phase minimum corresponds closer to the data obtained from the P mode. It is therefore expected that the phase at the minimum reflects the material properties more closely than the frequency at which this occurs.

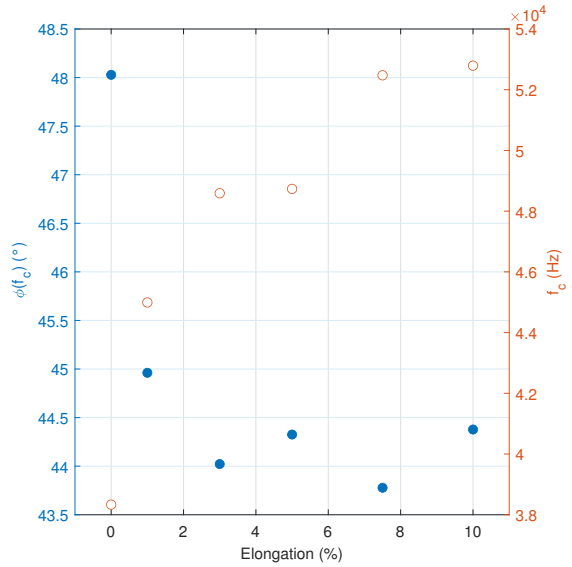

Figure 6.8: Relation of the critical frequency and corresponding phase versus elongation.

6.3 Magnetic hysteresis loops

6.3.1 High field

To validate the claim made in the previous paragraph the magnetization of the elongated specimen were measured using a vibrating sample magnetometer (VSM). A graph of the hysteresis loop can be seen in figure 6.9. The two curves are from the magnetization parallel and perpendicular to the field. Since the sample is put parallel to the field, the perpendicular component is near zero (less than 1% of the parallel field). Two of the measurements were conducted with the field parallel to the width of the strip, denoted by 90°. The rest of the measurements were with field parallel to the length, the same direction as the elongation. From the plot the maximum relative differential susceptibility, coercivity and remanence were obtained, with the used points coloured blue, and tabulated in table 1. The maximum magnetic moment was for all samples found to be close to 1.38 MA/m, with slightly decreasing values with increasing pre-strain.

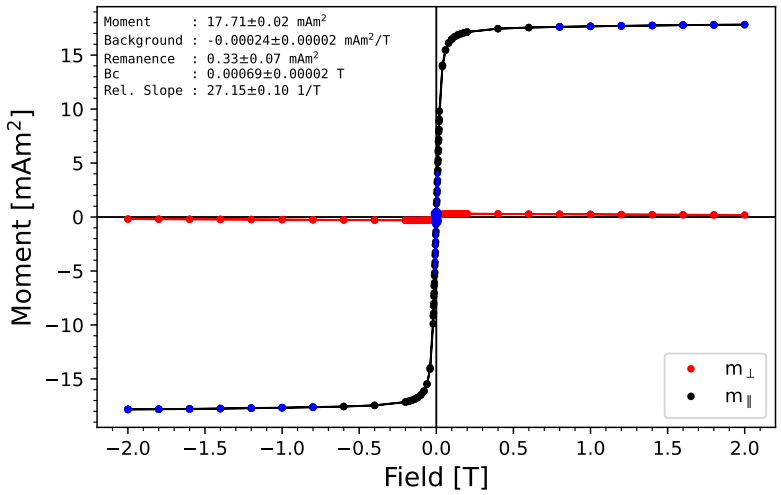

Figure 6.9: Hysteresis loop of the undeformed material in the length direction.

Elongation	Susceptibility	Moment (MA/m)	Coercive field (T)	Remanence (kA/m)
0%	47.60(1)	1.395(8)	0.00069(2)	26(6)
0% (90°)	46.98(1)	1.399(8)	0.000805(9)	31(5)
1%	41.15(4)	1.382(8)	0.0016(1)	54(4)
5%	37.91(2)	1.378(8)	0.00193(7)	60(5)
10%	38.30(1)	1.383(8)	0.00202(8)	62(4)
10% (90°)	47.76(2)	1.377(8)	0.001404(6)	55(6)

Table 1: Results from the high field VSM measurements.

And indeed, the susceptibility (and hence permeability) decreased significantly already with small strains and decreased much less upon further straining. The coercive field increases, indicating hardening of the magnetic properties, as should be expected from an increase in dislocation density from plastic strain. The remanence also increases noteworthy enough, in contrast to most of the findings of others [6, 11, 21]. The non-linear relation of permeability with strain can be explained by that the dislocation density increases quickly at low strain and much slower at higher dislocation densities and secondly because the inverse of permeability and the coercive field is proportional to the square root of dislocation density [11]. Interestingly enough, the permeabilities found were much lower than the values found in literature. Values of the maximum relative permeability for AISI 420 were reported to be 450 or 950, depending on the annealing procedure [22, 23]. Two other measurements on the permeability, using a different VSM (see section 6.3.4) and an inductance method (see figure 5.5), yield 27.2(4) and $1.1(1) \cdot 10^2$ respectively. The situations were slightly different in all cases and the reason for the discrepancy between the measurements is not clear. However, they are all much lower than literature. The reason for the large deviation from literature could be that the material has a different processing steps and hence harder magnetic properties

In the unstrained state the material is relatively isotropic permeability wise. After 10% elongation there is clear anisotropy in the permeability. Interestingly, the permeability at 90° to the tensile direction at 10% is higher than the permeability without deformation. This effect can be explained by that upon unloading, the regions with relatively high dislocation density remain in tension, while the regions with low density are compressed because the total internal stress should vanish [11]. Regions with low dislocation density are also regions in which domain wall motion occurs primarily. The residual compression of the material interacts with the permeability via magnetostriction, making magnetization more difficult in the parallel direction and easier than in the perpendicular direction. However, other researchers have concluded that the magneto-mechanical coupling is not responsible for the observed changes in magnetic properties [21]. Instead, they suggest that the formation of dislocations is anisotropic and that more dislocations form in the perpendicular direction during uniaxial loading. In any case the effect is that 90° walls will move before 180° walls, which is visible in the differential permeability curve as a second peak. Plots of the differential permeability curves are given in figure 6.10. As can be seen, the 10% strain shows asymmetric behaviour, which might be due to the separation of 90° and 180° wall movement. This effect was also visible in the 1% pre-strained specimen. In our case this effect is then small compared to that found in [11] and the effect might be the reason for the increase of the remanent field with elongation, as when the permeability reaches it's peak later, the hysteresis loop opens more, giving rise to a higher coercivity and remanence.

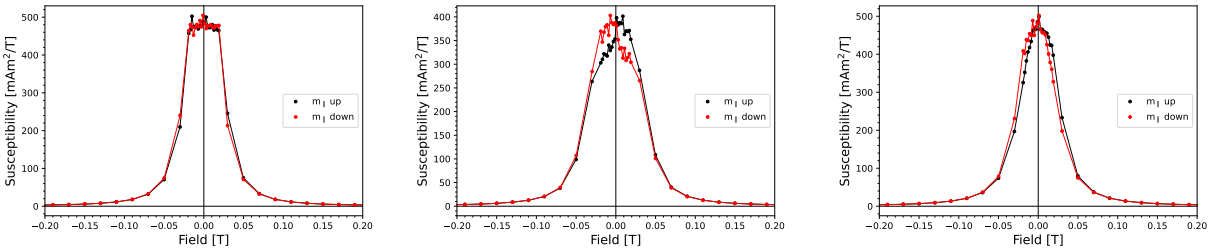

(a) 0% strain (b) 10% pre-strain (c) 10% pre-strain perpendicular

Figure 6.10: Susceptibility slopes, indicating different magnetization behaviours.

J.M Makar and B.K Tanner found a linear relation of the coercive field with pre-stress [21]. A plot of the coercive field against the pre-stress is given in figure 6.11 and can be seen to be indeed roughly linear.

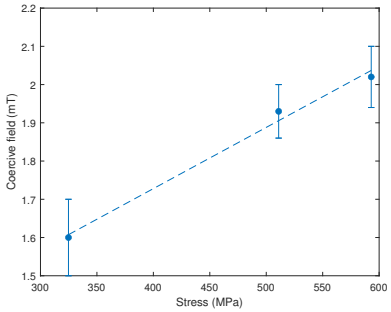

Figure 6.11: Linear relation of pre-stress versus coercive field

6.3.2 Rayleigh region

A situation more representative of the sensor can be created with a lower exciting field as the sensor field is expected to be between 630 A/m (0.8 mT) and 1260 A/m (1.6 mT), given two times 0.18 A with 35 windings over 1 cm, with the field combining in the strip for double the field strength. For this, a field of 1.6 mT was applied after demagnetizing with the VSM from the high field regime. Two susceptibilities are distinguished here: the initial susceptibility χ_i, obtainable from the slope at the turning point, and the average susceptibility χ_a, which is the time-averaged permeability under excitation of a sinusoidal field. Figure 6.12 shows the loop and it's slope at low field for the undeformed material in the length direction. From the slope can be seen that the susceptibility varies mostly linearly with field strength, according to the Rayleigh region. A Rayleigh hysteresis loop is plotted over the measured hysteresis loop in red. The two susceptibilities, the Rayleigh constant and the coercive field have been tabulated in table 2. The remanence was chosen to be omitted due to the loop being shifted vertically, giving uncertain values.

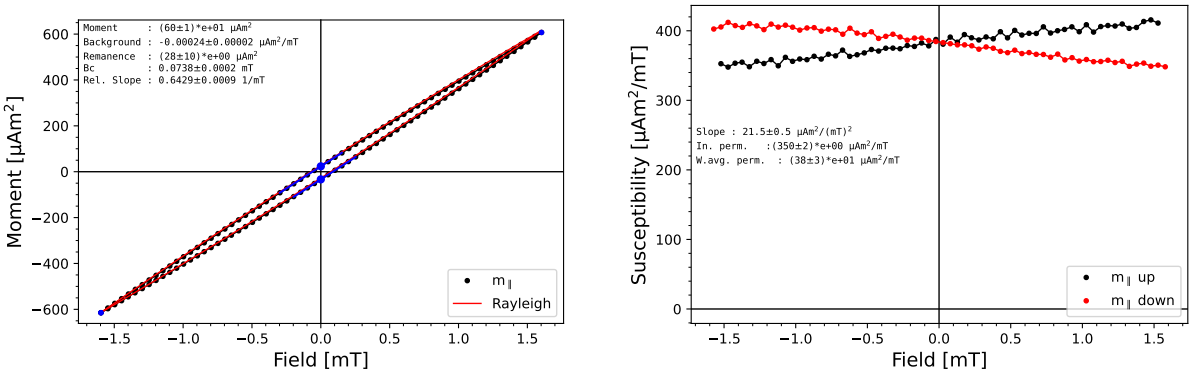

Figure 6.12: Low-field hysteresis loop (left) and it's slope (right) for the undeformed material.

From the data can be seen that the susceptibility is lower in general compared to the high field and also shows more change due to elongation. In this case the perpendicular direction at 10% strain has only a slight increase in initial permeability while a relatively large increase in the Rayleigh constant with respect to the parallel direction. In the conventional view of magnetization by domain wall movement, the initial permeability is the reversible part and

Elongation	χ_i	η (mm/A)	χ_a	Moment (kA/m)	Coercive field (mT)
0%	34.7(2)	2.67(6)	38(3)	47(1)	0.7380(2)
0% (90°)	34.2(7)	2.07(5)	37(3)	46(2)	0.0597(2)
1%	28.0(2)	1.232(3)	30(2)	37(2)	0.04297(6)
5%	25.8(3)	0.96(1)	27(1)	34(2)	0.0431(3)
10%	25.6(1)	1.00(3)	26(1)	34(2)	0.0410(1)
10% (90°)	26.9(2)	3.04(1)	30(4)	39(2)	0.1000(4)

Table 2: Results from the low-field (16 mT) VSM measurements.

hence a measure of how far apart pinning sites are. The Rayleigh constant is the first order term of irreversible magnetization. We can see that both the initial permeability and the Rayleigh constant decrease with increasing strain due to the increase of dislocations [8].

Since the initial permeability is roughly equal in both directions for the 10% elongation, it is suspected that the amount of dislocations in both directions is roughly the same. The larger Rayleigh constant in the perpendicular direction can be explained with the residual compressive stresses, favouring wall growth in the perpendicular direction and causing more irreversible wall displacements.

The coercive force can be seen to decrease with increasing elongation. This is because at this low field the nonzero interception with the horizontal axis (and also the vertical axis) depends heavily on the irreversible part of the magnetization, that is, the Rayleigh constant.

6.3.3 Sensor loop

With the sensor in P mode an approximate hysteresis loop of the strip can be created by graphing the integrated test voltage against the reference voltage while correcting for the signal without strip. This is done in figure 6.13a for 1000 Hz at various input voltages. As can be seen, these loops looks similar to the Rayleigh loop seen in last paragraph. At lower reference voltage the curve becomes slightly more horizontal, which is the normal behaviour for Rayleigh loops. In 6.13b such hysteresis loops are plotted for various frequencies at 20 V. The figure shows that the loop becomes relatively thicker at higher frequencies, indicating more losses. Higher frequencies also cause the loop to become more horizontal, as the reference voltage reduces at higher frequency due to the coil resisting current. The high frequency loop of 100 000 Hz can no longer be clearly associated with a Rayleigh loop due to the phase getting shifted too significantly.

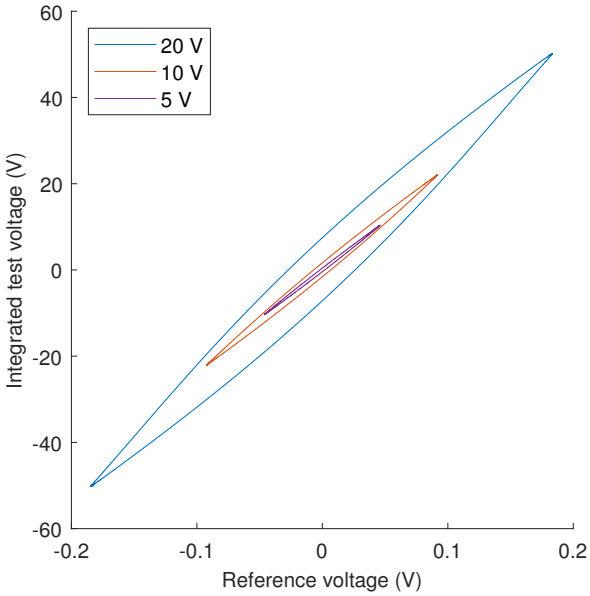

(a) Hysteresis loops at 1000 Hz for 5,10 and 20 V.

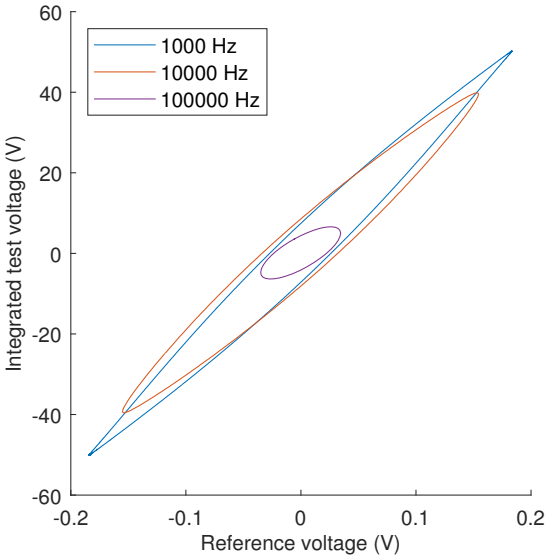

(b) Hysteresis loops at 20 V for 1000, 10000 and 100 000 Hz.

Figure 6.13: Sensor hysteresis loops at various voltages and frequencies.

Also for the deformed samples such loops were made and fitted with a second order polynomial from which an 'initial permeability' and 'Rayleigh constant' can be obtained. These parameters do not reflect the true material properties due to the unknown scaling in the voltages to field strength, the inhomogeneous field and the unknown volume of material in the sensor. By normalizing to the undeformed sample this unknown scaling is mitigated. Figure 6.14 shows a comparison between the different normalized permeabilities measured with the VSM, the sensor output in P mode and the obtained normalized initial susceptibility from the sensor loops. As can be seen, all the VSM measured permeabilities drop less quick with deformation than the sensor output. This suggests that either the field from the VSM was too high or the model is far off with the predictions, as the predicted sensor output scales with the permeability in such a way that the prediction will always lie above the normalized permeability. The sensor susceptibility indicates a way quicker drop in susceptibility such that if such permeability is used the prediction will line up much closer.

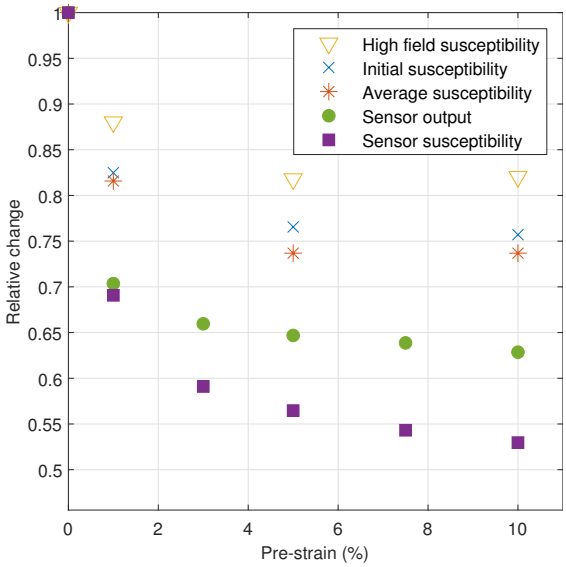

Figure 6.14: Normalized permeability and sensor output.

6.3.4 Linear regime

As seen in figure 6.14 the permeability showed a bigger initial decrease with a lower field so, based on extrapolation of this and on the sensor susceptibility showing the same trend, an exciting field of around 4 mT was chosen to be investigated further. As a result the magnetization was indistinguishable from linear, which means the permeability took on a constant value. The obtained relative susceptibility can be seen in table 3.

Elongation	χ
0% (High-field)	26.2(4)
0%	19.7(2)
1%	18.8(2)
5%	17.8(3)
10%	17.7(2)

Table 3: Results from the low-field (4 mT) VSM measurements.

The difference between the different elongations is much smaller, with at most a 10% deviation, in contrast with the sensor susceptibility which differs by at least 30%, even when the sensor is actuated by only 5 V. Moreover, the linear behaviour is not visible in the sensor, not even at 5 V.

A different VSM was used this time, requiring a sample size of 4 by 4 mm, which measured a high field (0.4 T) relative maximum differential permeability of 27.2(4). The discrepancy between the two measurements with around factor two is quite noticeable. An initial objection could be that this might be due to demagnetizing effects, as the smaller sample is expected to have a larger demagnetizing field. However, the demagnetizing effects should be negligible for the dimensions in question. No satisfactory explanation for the deviation has been found. The VSM in question showed less precision with low fields and suffered from

some actuation problems which were most pronounced in the low field as well. Because of this, the low-field measurements might not have sufficient resolution to show hysteresis. The VSM was well calibrated in the high field, so the high field result should not be due to a faulty device.

6.4 Grains

Figure 6.15 shows the image quality map of the EBSD measurements, where dark is poor quality and with grains indicated by colour. Carbides are visible as dark specks. In figure 6.16 the grain size and grain orientation are plotted. There is not an immediately clear trend in in the graphs across the different pre-strains. The area fraction of larger grain sizes decreases for 1% and 5% but for 10% there is a larger area taken up by large grains. The variation in the data might be due to a small sample size, especially for large grains. Grain orientation seems to be mainly in the vertical direction, which was taken to be the rolling and tension direction, except for 5%. The orientation of the sample in the mount and the mount in the EBSD machine were controlled manually and hence an error can not be excluded. There does seem to be a trend where the orientation takes on local minima around 30, 60, 90, 120 and 150°. This trend seems to be a characteristic of the delivered material and might be due to the rolling process. Alternatively this trend could be due to the software. However, the changes in directionality and size seem too small and devoid of clear increasing or decreasing trend to be the cause of the reduction in inductance.

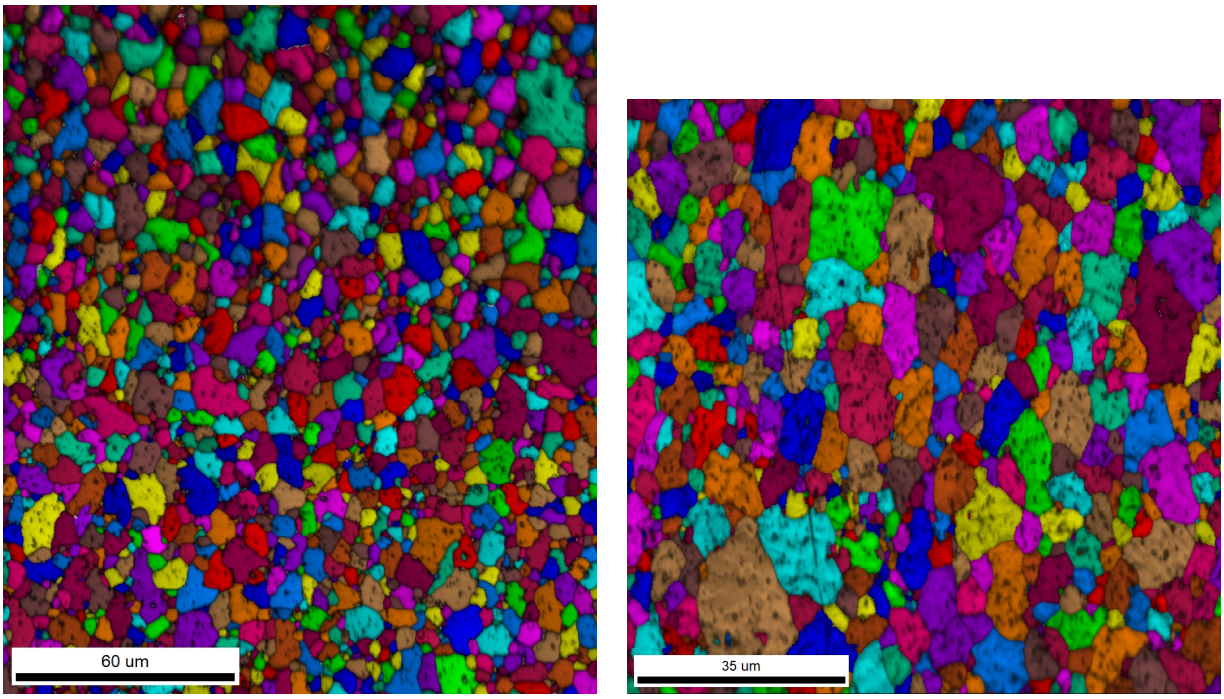

(a) 0% pre-strain (b) 10% pre-strain

Figure 6.15: EBSD image quality (dark regions are poor fit quality, indicating boundaries, carbides and other defects) together with grain color highlights.

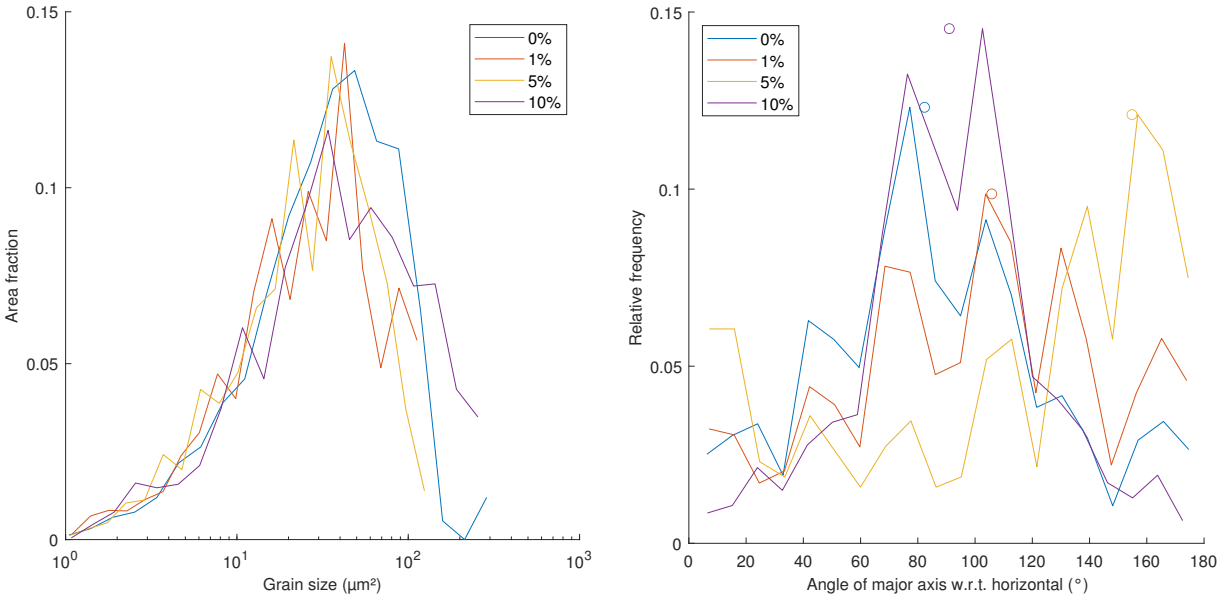

Figure 6.16: Grain size and ellipse orientation for different pre-strains, circles of the corresponding color indicate the circular mean.

6.5 Dislocation density

Various sources label the dislocation density as a major factor in the change of permeability [8, 9, 11, 24]. EBSD measurements are commonly performed to get a measure of the dislocation density by means of the kernel average misorientation (KAM) [25, 26]. As can be seen in figure 6.17, higher pre-strain shifts the probability distribution to higher deformation angles as expected. Higher elongation leads to increasingly higher average deformation angle. Dislocations can be distinguished in two categories: geometrically necessary dislocations (GND) and statistically stored dislocations (SSD) [27]. The GND density, which can be calculated in OIM as well, is related to KAM and shows the same trends. If the KAM is an accurate measure of the dislocation density, we must conclude the susceptibility does not have a straightforward relation with the dislocation density since the susceptibility flattens out at higher strains while the KAM increases faster than linearly with elongation. The dislocations formed may differ, as it is found that at low strains the dislocations remain isolated while at larger strains they form tangles, which interact more strongly with domains [11, 21].

From the KAM plots the directionality can be analysed using the directionality plugin from FIJI, of which the results are shown in figure 6.18. As can be seen, no clear directionality is visible, which does not support the notion that the dislocations occur anisotropically. If anything, at 10% strain the dislocation density seems slightly lower in the direction perpendicular to the strain (horizontal), in contrast to the prediction made by [21]. It is however likely that the directionality of dislocations only becomes apparent at smaller scales and that EBSD is not well suited for this.

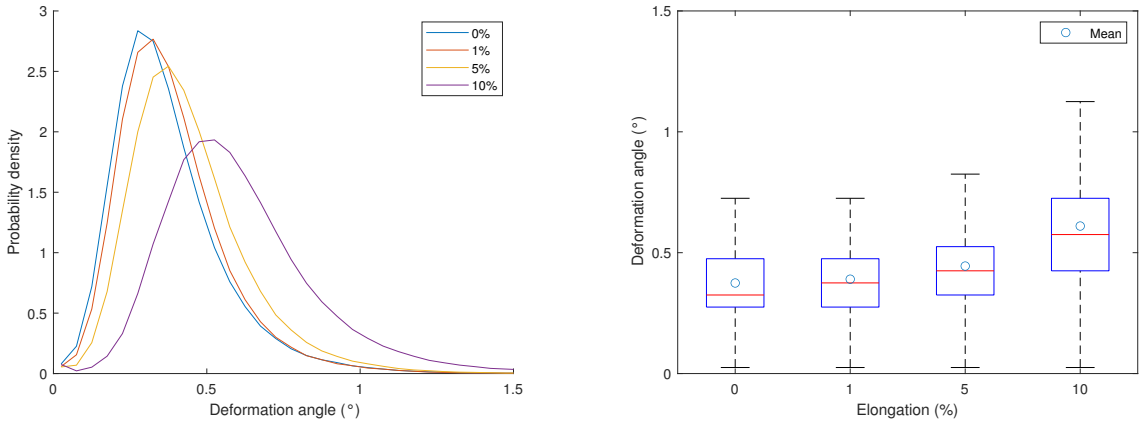

Figure 6.17: Kernel average misorientation for various pre-strains.

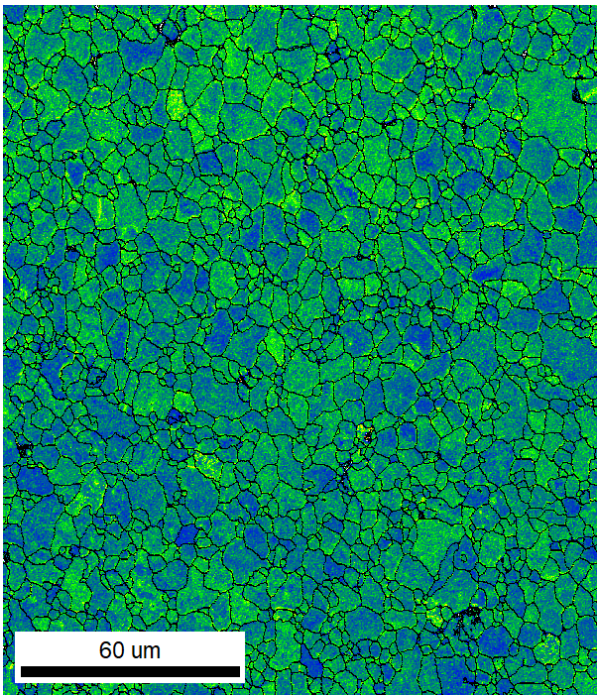

(a) KAM at 0% strain

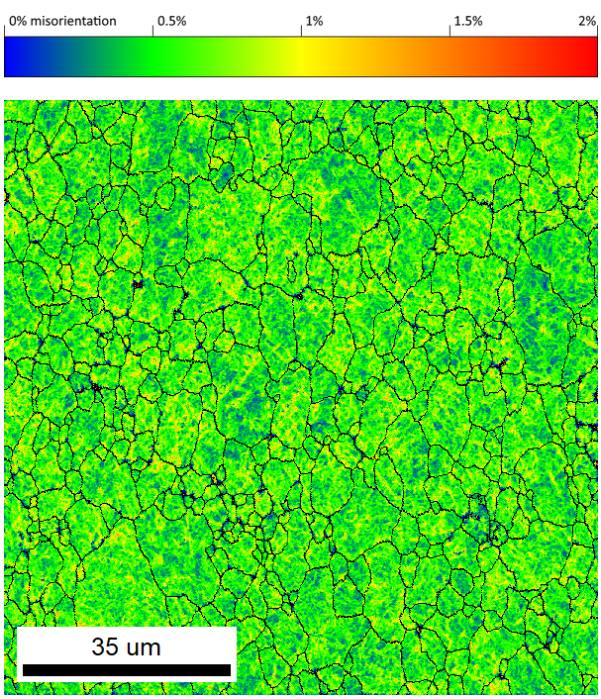

(b) KAM at 10% strain

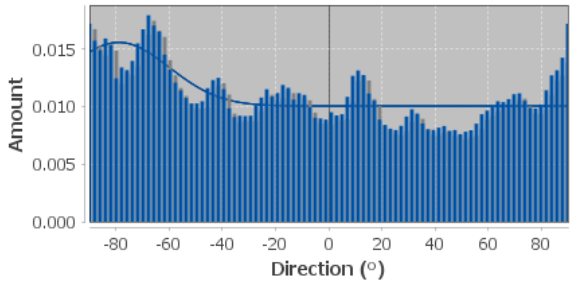

(c) Directionality at 0% strain

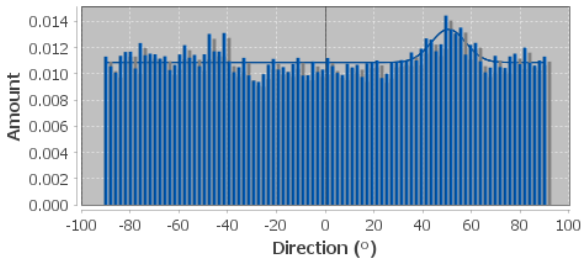

(d) Directionality at 10% strain

Figure 6.18: Kernel average misorientation for various elongation. The grain boundaries are highlighted in black. The directionality of the KAM data is show below with angles in the mathematical sense, 0° pointing to the right.

6.6 Magnetic domains

Figure 6.19 shows succesful MFM images of an undeformed sample. The carbides are well visible on the height maps, the grains are also slightly visible due to the difference in polishing speed from the crystal orientation. Lastly, the speckles, most clearly seen on 6.19c are believed to be either dust or OP-S particles as they diminish with additional treatment.

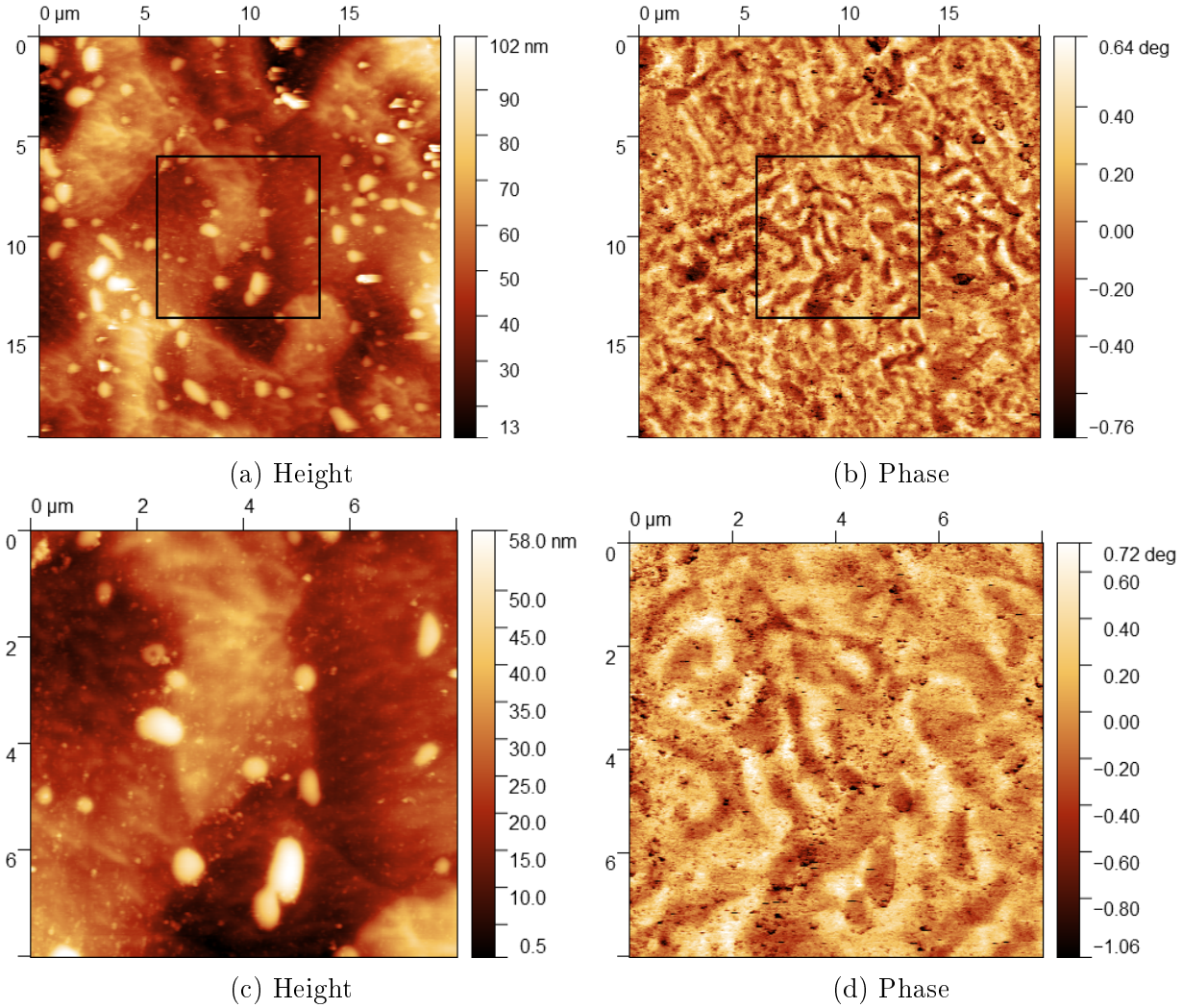

(a) Height (b) Phase

(c) Height (d) Phase

Figure 6.19: MFM images of a piece of undeformed material, (c,d) are the magnified regions inside the black square in (a,b).

Figure 6.19 shows the relative phase and some characteristic features can be identified, such as a group of alternating light and dark regions in the middle, consisting of three light and two dark parallel strips, signifying 180° domains. Note that the contrast is not high enough to discern domain walls. Additionally, some directionality in the data can be spotted, see figure 6.20b. There seems to be a roughly 90° spacing between peaks, as should be expected from ferrite [8]. Figure 6.20a shows the phase with highlighted grain boundaries and carbides, which were identified by eye. Near grain boundaries the phase shifts often

looks discontinuous and sometimes even aligned with the boundary, as is to be expected of domain walls. Most of the domains in question seem to be up to 0.5 µm wide and up to 4 µm long. The carbides also seem to influence the boundary configuration in the sense that regions carbides discontinue boundaries and distort them from the 180° configuration. Higher pre-strains, in figure 6.21, show a decrease in domain size from 0% onwards. A quantitative analysis is not performed in this case as the image resolution varies and due to a lack of domain classification methods.

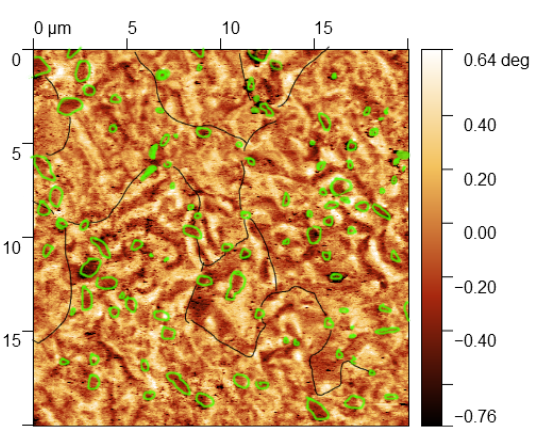

(a) Phase with overlay of grain boundaries (black) and carbides (green).

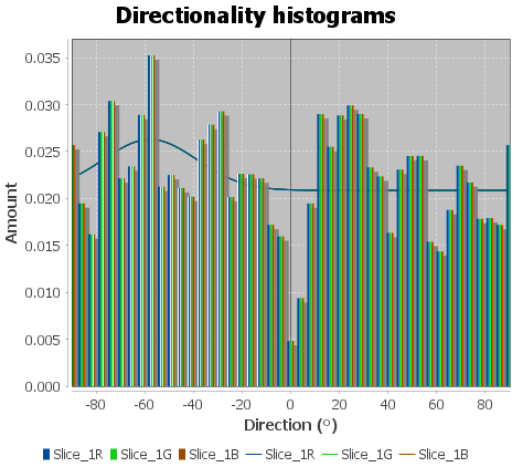

(b) Directionality of phase data.

Figure 6.20: Analysis on MFM images

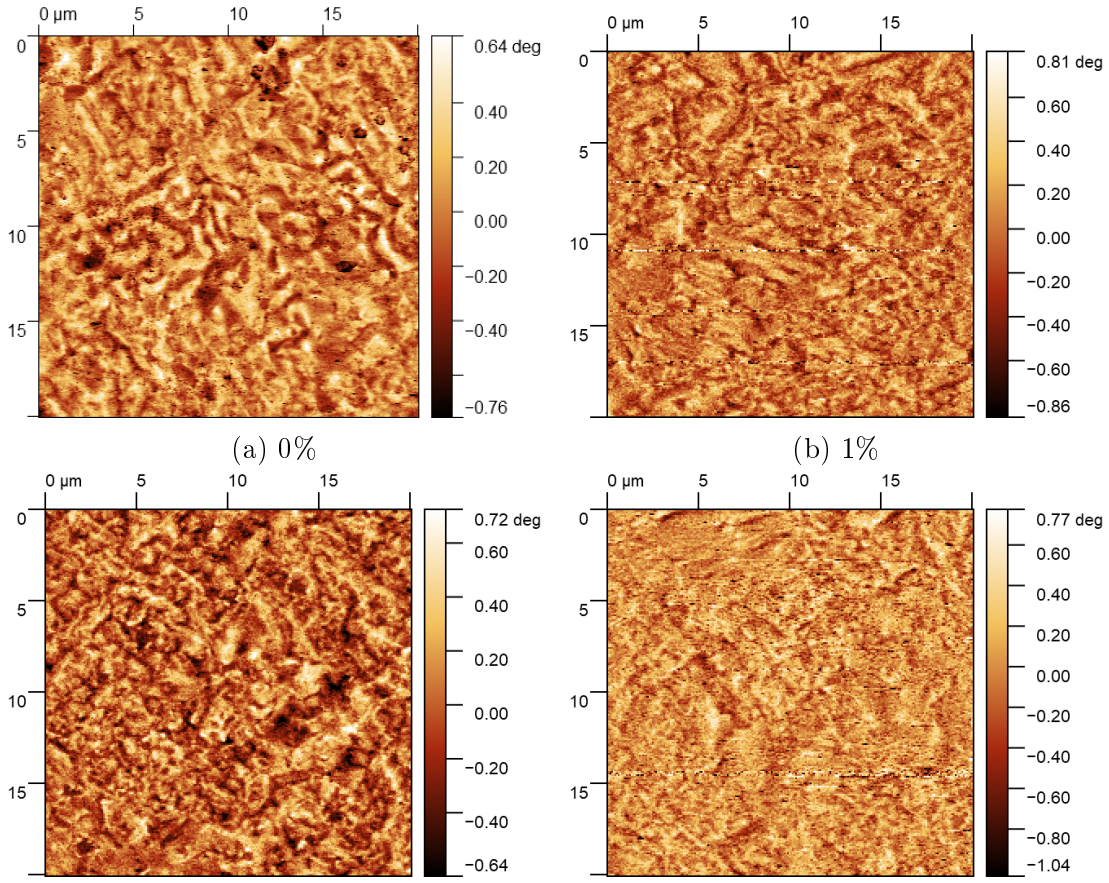

(a) 0% (b) 1%

(c) 5% (d) 10%

Figure 6.21: MFM images of various strains in the horizontal direction.

6.7 In-situ measurements

In figure 6.22 a plot of the loading and the sensor output can be seen. To calculate the stress the immediate cross sectional area was required, which was obtained from the relations 4.1.

For the permeance mode all the frequencies gave roughly the same output and the phase was also seen to vary simultaneously with the gain. To investigate all the effects further, two pure sine tests of 5 V and 20 V were conducted at 1000 Hz, which allowed for better control over the amplitude and investigation of the sensor hysteresis loops. This time the holding times were omitted. In 6.23a the inductance up to 2% strain is plotted against the immediate stress. The 5 V curve has points labelled in chronological order. From A to B, in the elastic regime, the inductance monotonically decreases for the 5 V test but the 20 V curve can be seen to first increase before decreasing. The increase can be readily attributed to magnetostriction and the decrease at higher stresses is a common phenomena for iron called the *Villari reversal*, where the magnetostriction changes sign [9, 28, 29, 30]. The absence of an increase and the difference in inductance for the 5 V case could be due to handling of the strip to place it in the tensile bench and sensor after demagnetization or simply due to the different field strength. From B to C the material plastically deforms,

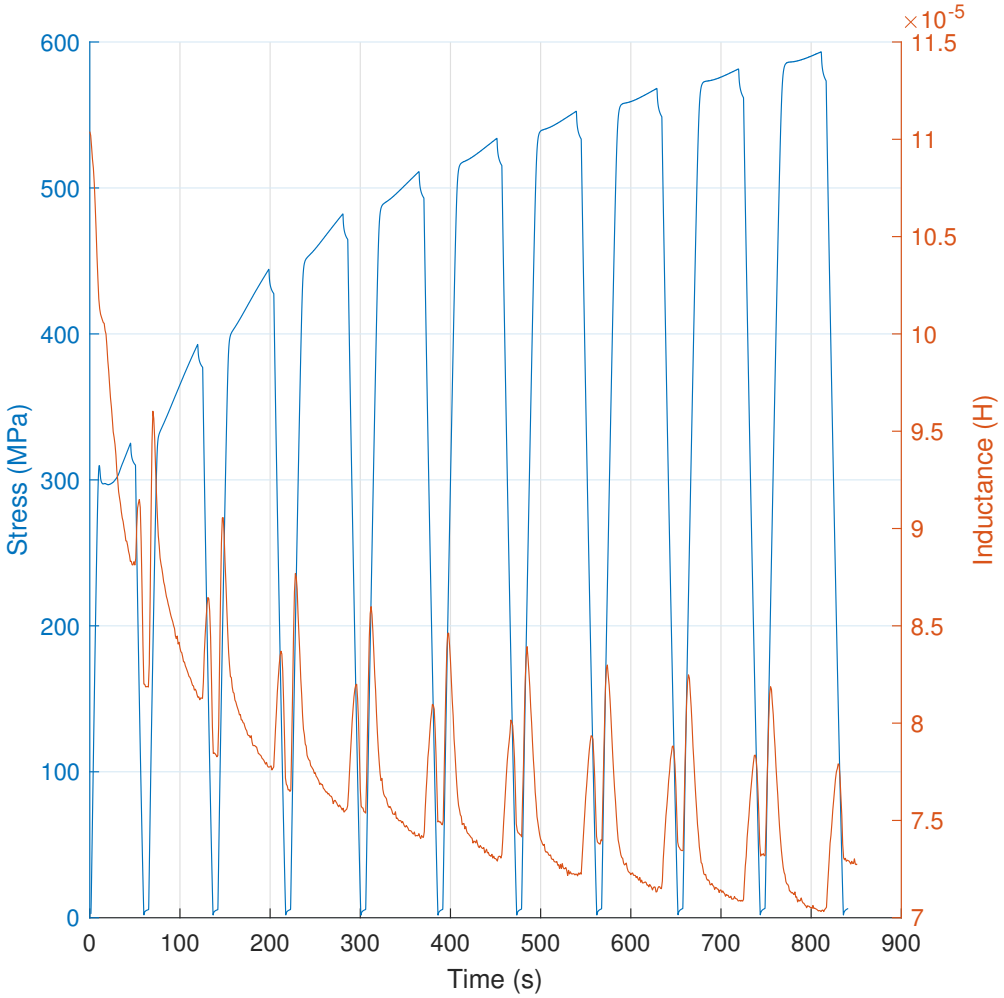

Figure 6.22: Cyclic elongation stress and sensor permeance mode output at 500 Hz.

increasing the dislocation density which decreases the inductance. Unloading from C causes the inductance to slightly increase before drastically decreasing. This decrease is believed to be due to the residual compressive stresses. Why the hysteresis upon reloading occurs is not clear but most likely not due to the hysteresis in the stress-strain curve, as the width and thickness change are so small that the influence is negligible. Ewing also reported a similar hysteresis in loading and unloading [30]. In figure 6.23b the peak inductance at loaded and unloaded is set out against the stress at the corresponding fully loaded state, motivated by [21, 24]. The evolution of inductance with pre-stress exhibits a clear difference between loaded and unloaded states, regardless of the applied field strength. This can be due to various effects like the residual compressive stress growing slower or the nonlinear scaling of magnetostriction with stress. Another striking effect is that the inductance difference between the two curves is different based on if the curve is loaded or unloaded. This might be because the magnetostriction depends on the magnetization [30]. The result where the difference in magnetization for two field strengths for tensile stress is higher than compressive stress can also be found by the Jiles-Artherton model, see appendix B [28].

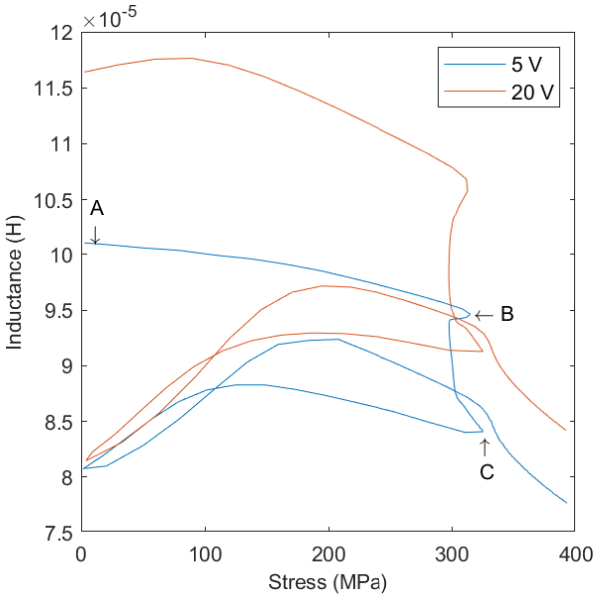

(a) Stress against inductance up to 2% engineering strain.

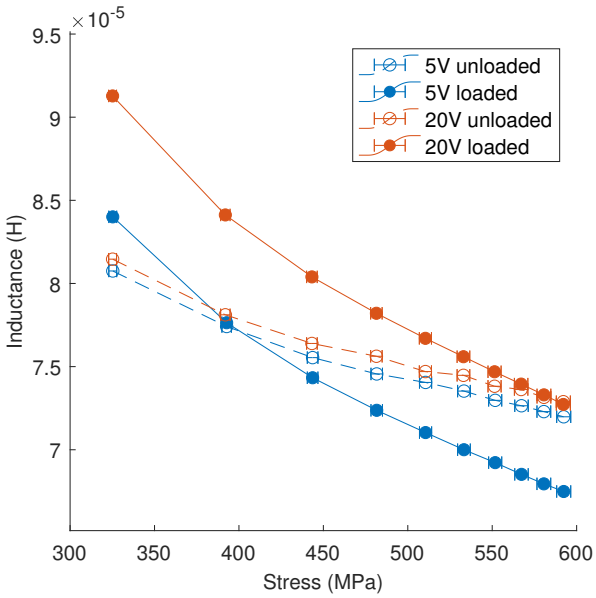

(b) Peak stress against inductance for fully loaded and unloaded points.

Figure 6.23: Comparison of 5 V and 20 V at 1000 Hz.

The stress at the inductance peaks during unloading and loading is plotted in figure 6.24 and can be seen to be roughly constant over the different cycles, especially for 5 V, indicating this is not a transient effect due to for example the loading speed but rather magnetostriction.

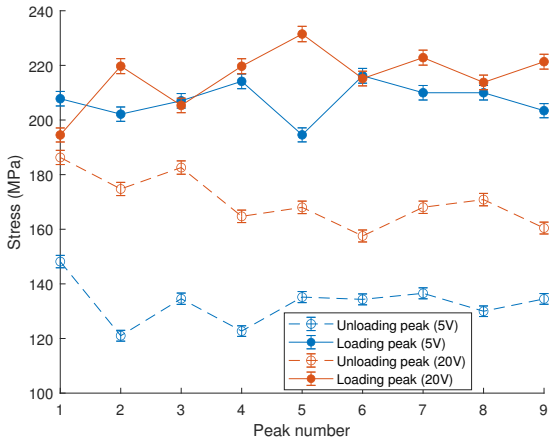

Figure 6.24: Stress values of loading and unloading peaks.

The EC mode does have similar output, as seen in figure 6.25. Loading and unloading has roughly the same effect on the inductance. However, the inductance can be seen to increase after some time. This can be attributed to the material width decreasing. In this case the phase does show significant changes. At lower frequencies the phase increase with strain, and at higher frequencies the phase decreases with strain. These large trends are

all expected geometrical phenomena as observed in figure 6.4. In figure 6.26 the minimum phase and the corresponding frequency is plotted, in this case roughly the same observation as before, for figure 6.8, can be made. The phase minimum flattens out after multiple cycles while the critical frequency continues to change, attributable to the change in width. To isolate the true effects a proper model is required to correct for the shape change.

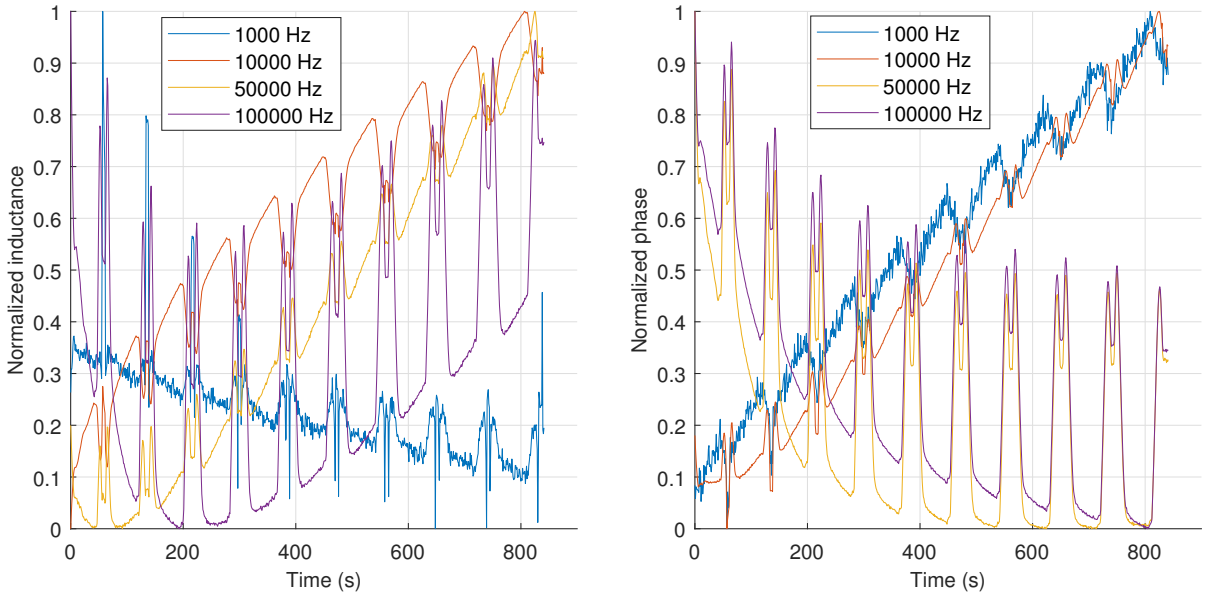

Figure 6.25: EC signal at various frequencies.

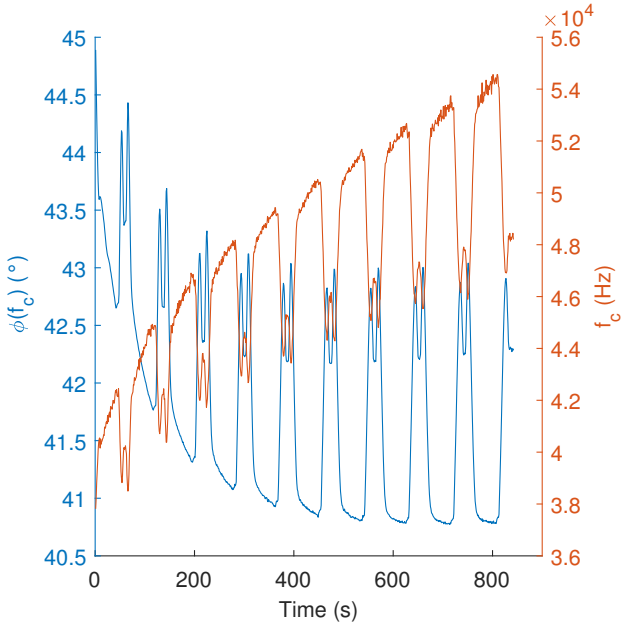

Figure 6.26: Minimum phase and corresponding critical frequency against time.

7 Conclusion

The connection between the microstructure and macrostructure has been found to be very complicated due to the many unknown relations between phenomena. For AISI 420 the main influences on the sensor output were found to be the dimensions, the initial work hardening and lastly the residuals stresses. The output depending on dimensions was analysed and a gyrator-capacitor model of the sensor was created. A good fit of the permeance mode model was found with an adjusted R-squared of 0.998. Work hardening was introduced using tensile stresses and it was found that the sensor has a clear response on mainly the initial deformation. Measurements on the magnetic properties with a VSM show similar trends but a different initial change with pre-strain. Moreover, various measurements have been done on the susceptibility, resulting in values ranging from $27.2(4)$ to $1.1(1) \cdot 10^2$. No significant resistivity variation was found and the microstructural changes like grain size and grain orientation do not show a clear relation with amount of pre-strain. The KAM clearly increases with strain, however the mean and median do not show a clear relation with the sensor output. MFM imaging has been applied and a refinement of the domains can be spotted. In-situ tensile tests show the magneto-mechanical coupling and the Villari reversal due to stress. Residual compressive stresses are suspected to be present and cause an additional decline in the sensor inductance. This effect would also explain the directional anisotropy found in the ex-situ VSM tests.

7.1 Recommendations

Determining the microstructure with the sensor output is as of yet not feasible and requires at least more research. To link the sensor output and the microstructure it seems multi-domain simulations of both the sensor and the material are the way forward. The EC mode is more complicated than the P mode and a proper model might require modelling the parasitic capacitance with damping. Because of this and because the P mode is better understood and has more volume in the sensor, it might be worthwhile to do (in-line) measurements with the P mode instead, at least for now. Besides that, if the signal generator is to operate continuously in-line, a small investigation on whether the output changes over time might be fruitful.

7.2 Acknowledgements

Firstly I'd like to thank my supervisors Yutao, Celal and Redmer for helping me regularly with the project. I'd like to thank Peter Bax for help with the sensor model, Leon Abelmann and Jacob Baas for doing VSM measurements, Wei Zhang for EBSD measurements and Sytze Tirion for succesful MFM measurements. I also am grateful for the support of my colleagues at Philips and all the other people who helped with the project.

References

[1] H. Kwun and G. L. Burkhardt, "Effects of grain size, hardness, and stress on the magnetic hysteresis loops of ferromagnetic steels," *Journal of Applied Physics*, vol. 61, no. 4, pp. 1576–1579, 1987. [Online]. Available: https://doi.org/10.1063/1.338093

[2] M. Aghadavoudi-Jolfaei, J. Shen, A. Smith, L. Zhou, and C. Davis, "Non-destructive measurement of microstructure and tensile strength in varying thickness commercial dp steel strip using an em sensor," *Journal of Magnetism and Magnetic Materials*, vol. 473, pp. 477–483, 2019. [Online]. Available: https://www.sciencedirect.com/science/article/pii/S0304885318325812

[3] K. G. Bøving, *NDE handbook: non-destructive examination methods for condition monitoring*. Elsevier, 2014.

[4] L. Zhou, "Non-destructive characterisation of steel microstructures using electromagnetic sensors," 2015.

[5] X. Hu, Z. Fu, Z. Wang, and J. Zhang, "Research on a theoretical model of magnetic nondestructive testing for ferromagnetic materials based on the magneto–mechanical coupling effect," *Journal of Physics D: Applied Physics*, vol. 54, no. 41, p. 415002, Jul. 2021. [Online]. Available: https://doi.org/10.1088/1361-6463/ac100c

[6] M. Domenjoud and L. Daniel, "Effects of plastic strain and reloading stress on the magneto-mechanical behavior of electrical steels: Experiments and modeling," *Mechanics of Materials*, vol. 176, p. 104510, Jan. 2023. [Online]. Available: https://doi.org/10.1016/j.mechmat.2022.104510

[7] R. Bozorth, *Ferromagnetism*, 8th ed. New York: Van Nostrand, 1951.

[8] S. Chikazumi, *Physics of Ferromagnetism*, 2nd ed. Oxford University Press, USA, 1997.

[9] B. D. Cullity and C. D. Graham, *Introduction to Magnetic Materials*, 2nd ed. Wiley, 1972.

[10] J. Baldwin, "Rayleigh hysteresis–a new look at an old law," *IEEE Transactions on Magnetics*, vol. 14, no. 2, pp. 81–84, Mar. 1978. [Online]. Available: https://doi.org/10.1109/tmag.1978.1059730

[11] J. Pal'a, O. Stupakov, J. Bydžovský, I. Tomáš, and V. Novák, "Magnetic behaviour of low-carbon steel in parallel and perpendicular directions to tensile deformation," *Journal of Magnetism and Magnetic Materials*, vol. 310, no. 1, pp. 57–62, Mar. 2007. [Online]. Available: https://doi.org/10.1016/j.jmmm.2006.07.029

[12] D. Griffiths, *Introduction to electrodynamics*, 4th ed. Pearson, 2014.

[13] P. Bax, "Modelling approaches for multi-domain systems," philips internal.

[14] S. Feng, "Characterization of steel material for shaving caps by means of magnetic measurements," 2018, philips internal.

[15] D. Hamill, "Gyrator-capacitor modeling: a better way of understanding magnetic components," in *Proceedings of 1994 IEEE Applied Power Electronics Conference and Exposition - ASPEC'94*, 1994, pp. 326–332 vol.1.

[16] H. Zhang, M. Tian, H. Li, L. Dong, and L. Sun, "Improved gyrator–capacitor model considering eddy current and excess losses based on loss separation method," *AIP Advances*, vol. 10, no. 3, p. 035309, 2020. [Online]. Available: https://doi.org/10.1063/1.5143172

[17] *Sandvik 6C27 strip steel datasheet*, Sandvik, Dec. 2020.

[18] Y. Pei, Private Communication, 2023.

[19] A. Hubert and R. Schäfer, *Magnetic Domains*. Springer Berlin Heidelberg, 1998. [Online]. Available: https://doi.org/10.1007/978-3-540-85054-0

[20] H. Hopster and H. P. Oepen, Eds., *Magnetic Microscopy of Nanostructures*. Springer Berlin Heidelberg, 2005. [Online]. Available: https://doi.org/10.1007/b137837

[21] J. Makar and B. Tanner, "The effect of plastic deformation and residual stress on the permeability and magnetostriction of steels," *Journal of Magnetism and Magnetic Materials*, vol. 222, no. 3, pp. 291–304, Dec. 2000. [Online]. Available: https://doi.org/10.1016/s0304-8853(00)00558-8

[22] P. Oxley, J. Goodell, and R. Molt, "Magnetic properties of stainless steels at room and cryogenic temperatures," *Journal of Magnetism and Magnetic Materials*, vol. 321, no. 14, pp. 2107–2114, 2009, current Perspectives: Modern Microwave Materials. [Online]. Available: https://www.sciencedirect.com/science/article/pii/S0304885309000079

[23] D. W. Dietrich, "Magnetically soft materials," in *Properties and Selection: Nonferrous Alloys and Special-Purpose Materials*. ASM International, Jan. 1990, pp. 761–781. [Online]. Available: https://doi.org/10.31399/asm.hb.v02.a0001093

[24] J. Makar and B. Tanner, "The in situ measurement of the effect of plastic deformation on the magnetic properties of steel," *Journal of Magnetism and Magnetic Materials*, vol. 184, no. 2, pp. 193–208, Apr. 1998. [Online]. Available: https://doi.org/10.1016/s0304-8853(97)01129-3

[25] J. Moerman, P. R. Triguero, C. Tasan, and P. van Liempt, "Evaluation of geometrically necessary dislocations density (GNDD) near phase boundaries in dual phase steels by means of EBSD," *Materials Science Forum*, vol. 702-703, pp. 485–488, Dec. 2011. [Online]. Available: https://doi.org/10.4028/www.scientific.net/msf.702-703.485

[26] A. Kundu and D. P. Field, "Geometrically necessary dislocation density evolution in interstitial free steel at small plastic strains," *Metallurgical and Materials Transactions A*, vol. 49, no. 8, pp. 3274–3282, Jun. 2018. [Online]. Available: https://doi.org/10.1007/s11661-018-4693-1

[27] A. Arsenlis and D. Parks, "Crystallographic aspects of geometrically-necessary and statistically-stored dislocation density," *Acta Materialia*, vol. 47, no. 5, pp. 1597–1611, Mar. 1999. [Online]. Available: https://doi.org/10.1016/s1359-6454(99)00020-8

[28] M. J. Sablik, H. Kwun, G. L. Burkhardt, and D. C. Jiles, "Model for the effect of tensile and compressive stress on ferromagnetic hysteresis," *Journal of Applied Physics*, vol. 61, no. 8, pp. 3799–3801, Apr. 1987. [Online]. Available: https://doi.org/10.1063/1.338650

[29] R. M. Bozorth and H. J. Williams, "Effect of small stresses on magnetic properties," *Reviews of Modern Physics*, vol. 17, no. 1, pp. 72–80, Jan. 1945. [Online]. Available: https://doi.org/10.1103/revmodphys.17.72

[30] J. Ewing, *Magnetic Induction in Iron and Other Metals*, ser. Electrician series. D. Van Nostrand Company, 1892. [Online]. Available: https://books.google.nl/books?id=OXq8zQEACAAJ

[31] C. Soyarslan, Private Communication, 2023.

[32] R. Blum, "Eddy current sensor in the 0.2 mm cap line," 2019, philips internal.

Appendix A Sensor Documentation

A.1 Sensor design

Section redacted.

Figure A.1: Schematic views of the sensor [31].

A.2 Circuit board

Section redacted

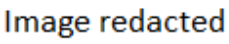

Figure A.2: Circuit board for the sensor [14].

A.3 Input and data acquisition

The output of the sensor are the voltages measured over the coils. These voltages can be compared to the reference signal and a gain and a phase can be found. For the data acquisition a National Instruments BNC2110 unit connected with a PCIe-6374 card was used and a RIGOL DG1022 for the signal generation. The conclusion of Roy Blum was that a sine or a superposition of sines at maximum voltage is best with regards to the errors [32]. By superimposing sines the error is affected minimally while increasing the amount of measurements done in a single run. Finding the gain and phase can be done using Fourier analysis on the signals and selecting the strongest signals. The complex Fourier output gives the gain and phase. Alternatively a least squares method can be used since the excitation frequencies are known. Both methods are roughly equal error-wise. A side effect of superimposing sines is that the voltage amplitude of an isolated frequency will decrease. It might be for example that if 20 frequencies are superimposed then the maximum voltage of 20 V will be attained when all the individual amplitudes are 1 volt. When the maximum signal is applied the maximum current through the coil was found to be at most 0.2 A but can be lower at high frequencies. Another effect of superimposing sines is that the input signal quality decreases when the frequencies have a large difference since the signal generator can only cache around 6000 points for the input signal. For example superimposing a 100 Hz sine with a 150 000 Hz sine means there are only four points per period of the latter sine. Lastly it must be noted that superimposing signals which are not integer multiples causes the superimposed signal to have a longer period. Because of this the quality can decrease quite quickly and using for example logarithmically spaced frequencies over larger ranges is not a good idea. Another effect found was that the signal generator could not properly handle prolonged operation with 20 V output and would output a signal differing somewhat from a sine.

A.4 Sensor output

The sensor data can be captured as the circuit impedance

$$Z = \frac{v_{test}}{i_{ref}} = \frac{v_{test}}{v_{ref}} \tag{A.1}$$

Where v_{test} is the instantaneous voltage over the receiving coil and i_{ref} and v_{ref} are the instantaneous current and voltage over the 1 Ω resistor. Given the input and output signals are sinusoidal with the same frequency, we can write

$$Z = |Z|e^{j\theta}, \tag{A.2}$$

with $|Z|$ the *magnitude* or *gain* of the impedance, often expressed in decibels as

$$Z_{dB} = 20\log(|Z|), \tag{A.3}$$

and $\theta = \mathrm{Arg}(Z)$ the argument of the impedance, which is the phase difference between input and output. The magnitude can also be divided by the angular frequency to obtain the

mutual inductance of the setup:

$$M = \frac{|Z|}{2\pi f}. \tag{A.4}$$

The advantage of this is that the output gives a horizontal line instead of diagonal when plotted as function of frequency, giving higher visual clarity for deviations of linearity. In figure A.3 typical sensor output can be seen. Plotted are the gains and phases with the EC and P mode for the sensor with and without a metal strip. As can be seen, if material is placed in the sensor, the gain is higher. This effect is much more noticeable in the permeance mode as the strip provides a good path for the horizontal magnetic flux, but not as good for the vertical flux. A noteworthy feature in the gain plot is that all the lines are approximately linear on the log-scale, except for part of the EC measurement with material. The phase plot for the EC measurement with the strip is also the most visually distinct, showing a local minimum and maximum, indicating loss due to eddy currents. The sensor output can be explained by an electronic equivalent circuit to some degree, see section 3.1 for more information on this. The frequencies were selected to give a relatively large range of values. The EC mode has some concentrated points around the phase minimum for extra detail. In later measurements the selected frequency points might change slightly to increase the desired detail in some regions. There are some small wobbles in the phase at low frequency for the P mode, this behaviour seemed to be mainly influenced by the superposition of the sines but a clear origin was not found after a short investigation.

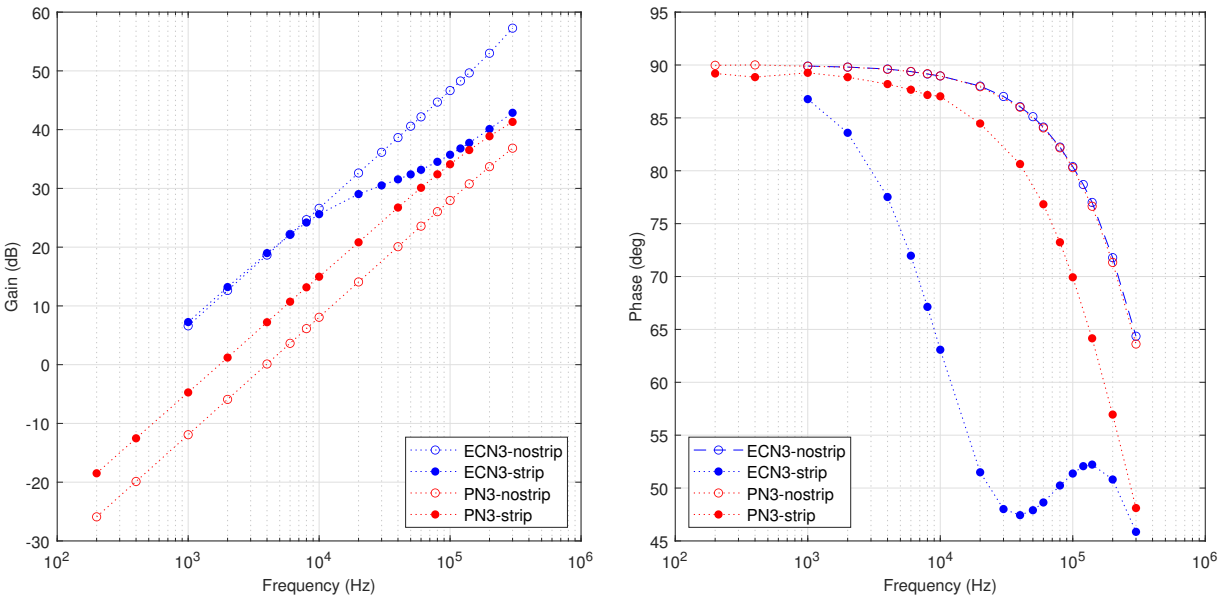

Figure A.3: Typical gains and phases from the sensor.

A.5 Measurement procedure

From measurements it was found that there are various sources which cause variation in the output. One of the biggest contributor was the height of the strip in the sensor. To

decrease this effect a simple strip guidance was present and a strip support was added, as can be seen in figure A.4 and A.5, preventing the strip from sagging and keeping the strip at roughly the same height in the sensor. Another effect with big impact was the method of demagnetization. Turning the demagnetization plate off while the strip is still on the plate leaves a random magnetization behind. Instead, the strip should be pulled away slowly. It was found that also the direction of this movement mattered, therefore for the rest of the measurements the strip was demagnetized by sweeping the length of the strip over the length of the demagnetization plate from right to left. Demagnetization is necessary to put the material in a neutral state before measurement and was also advised by Shiyu and Roy [14, 32]. The demagnetizing plate can be seen in figure A.6. Other effects like small horizontal shifts in location or rotations of the strip were found to be minor. To avoid large horizontal shifts, the location of measurement was denoted on the strip with a marker.

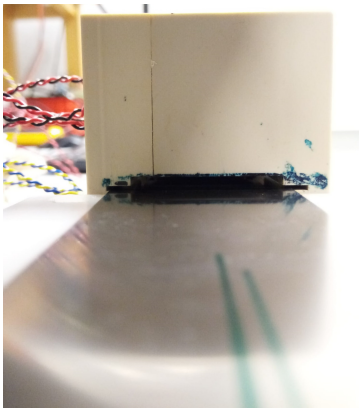

Figure A.4: Strip in sensor resting on side guidance.

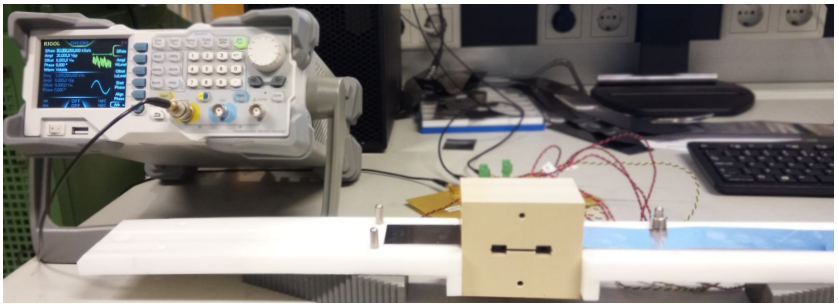

Figure A.5: Sensor (beige, middle) with strip support (white, sides) and signal generator (left).

Figure A.6: Demagnetization plate used throughout this research.

Appendix B Scripts

Script 1: Low Frequency Model (R)

```r
library(car)
setwd("C:/Users/320196768/Desktop/Project/R/Rdata")
PN3_width_thick = read.csv(file = 'PN3_width_thick.csv')
datf =data.frame(PN3_width_thick)
datf$Gain = 10^(datf$Gain/20) #db normal scale
datf$Width = datf$Width/1000 #mm to m
datf$Thickness = datf$Thickness/1000 #mm to m
mod_intercept = lm(Gain~0+Frequency,data=datf[datf$Width == 0&datf$Frequency <=2000,]) #intercept
datf$t2 = datf$Thickness^2
modfull = lm(Gain-mod_intercept$coefficients*Frequency ~ 0+Width:(Thickness+t2):Frequency,data=datf
    [datf$Width>0&datf$Frequency<=2000,])
mod500 = lm(Gain-mod_intercept$coefficients*500 ~ 0+Width:(Thickness+t2),data=datf[datf$Width>0&
    datf$Frequency==500,])
par(mfrow = c(2, 2)); plot(modfull); par(mfrow = c(1, 1))
par(mfrow = c(2, 2)); plot(mod500); par(mfrow = c(1, 1))
 outlierTest (modfull)
influence.measures(modfull)
 outlierTest (mod500)
```

Script 2: Jiles-Artherton Model (Matlab)

```matlab
a = 700; % A/m
alpha = 0.0003;
c = 0.02;
k = 300; % A/m
Ms = 1.38e6; % A/m
lamb0 = 0.00002;
lambt = 0.000005;
lambc = 0.00005;
stresst = 80*6.9*10^6;
stressc = -40*6.9*10^6;
for Hmax = 80*[4,8,16] % loop over 3 different signal strengths
    stress = 6.9*10^6*(-40:2:80);
    for i = 1:length(stress) % loop over various stresses
        M = Jiles_Artherton(Hmax,a, alpha, c, k, Ms, lamb0,lambt,lambc,stress(i), stresst , stressc);
        maxM(i)=max(M);
    end
    figure(1) % plot 'inductance' vs stress
    plot( stress /10^6, maxM/Hmax,'-',DisplayName=['H␣=␣' num2str(Hmax)])
    xlabel('Stress␣[MPa]')
    ylabel('MaxM/Hmax')
    hold on
    legend()
    grid on
end

t = linspace(0,1.25,7001);
H = Hmax*sin(2*pi*t);
M = Jiles_Artherton(16*80,a, alpha, c, k, Ms, lamb0,lambt,lambc,0, stresst , stressc);
```

```
figure(2)
plot(H,M)
xlabel('H field [A/m]')
ylabel('Magnetization [A/m]')

function M = Jiles_Artherton(Hmax,a, alpha, c, k, Ms, lamb0,lambt,lambc,stress, stresst, stressc)
    mu0 = 4 * pi * 1e-7; % H/m
    Man = 0;
    dMirrdH = 0;
    Mirr = 0;
    M = 0;
    He = 0;
    dMdH = 0;
    alpha_s = 0;

    t = linspace(0,1.25,7001); %signal that lasts 1.25 full cycles with 7000 points
    H = Hmax*sin(2*pi*t);
    delta = sign(cos(2*pi*t));
    n=2; %zeroth order or second order magnetostriction
    if n==2 && stress>0
        lamb = (3/2)*((lamb0-lambt)*(1-(stress/stresst)^0.5)+lambt);
    elseif n==2
        lamb = (3/2)*((lamb0-lambc)*(1-(stress/stressc)^0.5)+lambc);
    else
        lamb = lamb0;
    end

    for i = 1:length(H)-1
        alpha_s(end+1) = 3/2*lamb /(mu0*Ms^2) * stress*(M(i)/Ms)^n;
        He(end+1) = H(i + 1) + (alpha + alpha_s(i+1))* M(i);
        Man(end+1) = Ms * (coth(He(i+1) / a) - a / He(i+1));
        if (H(i+1)-H(i))*(Man(i+1)-M(i)) >= 0
            dMdH(end+1) = 1/(c+1)*(Man(i+1) - M(i)) / (k * delta(i+1) - (alpha + (n+1)*alpha_s(i
                +1))*(Man(i + 1) - M(i)))+c/(c+1)*(Man(i+1) - Man(i))/(H(i+1) - H(i));
        else
            dMdH(end+1) = c/(c+1)*(Man(i+1) - Man(i))/(H(i+1) - H(i));
        end
        M(end+1) = M(i)+dMdH(i+1)*(H(i+1) - H(i));
    end
end
```